

Nonlinear ultrasonic guided waves—Principles for nondestructive evaluation



Cite as: J. Appl. Phys. **129**, 021101 (2021); doi: [10.1063/5.0038340](https://doi.org/10.1063/5.0038340)

Submitted: 23 November 2020 · Accepted: 21 December 2020 ·

Published Online: 11 January 2021



[View Online](#)



[Export Citation](#)



[CrossMark](#)

Cliff J. Lissenden^{a)} 

AFFILIATIONS

Department of Engineering Science and Mechanics, Penn State, University Park, Pennsylvania 16802, USA

^{a)}**Author to whom correspondence should be addressed:** Lissenden@psu.edu

ABSTRACT

Research into the use of nonlinear ultrasonic guided waves for nondestructive evaluation is expanding at a high rate because of the great potential benefit that they possess for early detection of material degradation. However, development of inspection and testing strategies is complicated because (i) the underlying physical principles are complex, (ii) there is a broad spectrum of possible solutions but only a limited number that have been shown to be effective, and (iii) the nonlinearity is weak and thus its measurement is challenging. This Tutorial aims to provide a foundation for researchers and technology-transitioners alike, to advance the application of nonlinear ultrasonic guided waves and ultimately transform how the service lives of structural systems are managed. The Tutorial focuses on the physical principles of nonlinear ultrasonic guided waves leading to the so-called internal resonance conditions that provide a means for selecting primary waves that generate cumulative secondary waves. To detect material degradation, we are primarily interested in nonlinearity stemming from the material itself, which is represented as hyperelastic. For the special case of plates, internal resonance points have been identified and case studies are presented to illustrate some of the applications. The Tutorial has one new result not published in a research paper; finite element simulation of energy transfer from shear-horizontal primary waves to symmetric Lamb waves at the second harmonic.

Published under license by AIP Publishing. <https://doi.org/10.1063/5.0038340>

I. INTRODUCTION

Nonlinear ultrasonic guided waves have strong potential to shift the paradigm in lifecycle management of structural systems because they provide indications of incipient material damage, are sensitive to breathing cracks, enable access to otherwise inaccessible locations, and can propagate relatively long distances. However, to apply nonlinear ultrasonic guided waves as technology, the principles of their propagation in wave guides must be mastered. One does not simply couple transducers to the waveguide and turn on the amplifier. Rather, it is necessary to understand how wave interactions are manifested, how to maximize the nonlinearity to enhance the sensitivity of the measurement, and how to connect the apparent nonlinearity to the material characteristics of interest. *The objective of this Tutorial is to introduce the fundamental physical principles for nonlinear ultrasonic guided waves and their applications to nondestructive evaluation of structural components that also serve as the ultrasonic waveguide.*

A. Ultrasonic nondestructive evaluation

Ensuring the structural integrity of machines and structural components through some form of nondestructive evaluation

(NDE) is vital for safe operation of the mechanical and structural systems in which they function. This includes both nondestructive testing for quality assurance of new parts and nondestructive inspection, whether by interrupting the operational service of the asset or by on-line structural health monitoring. In fact, preventing failures that have severe consequences on safety is just part of the objective, as affordability is always a consideration. Just as designers balance performance, reliability, and cost within the uncertainties associated with service requirements, the operators balance monitoring costs, asset unavailability due to inspection, logistics and replacements within the uncertainties associated with operating conditions, material degradation, damage progression, and failure. Emerging NDE techniques can improve and even transform non-destructive testing and inspection paradigms. This Tutorial examines the principles that form the foundation for the use of nonlinear ultrasonic guided waves in NDE applications. As such, it does not describe specific applications or provide comparisons with other NDE technologies. The application of these principles to specific mechanical systems and comparisons to other available technologies are left to the reader or can be found elsewhere.

To address what is meant by the term *nonlinear ultrasonic guided waves*, we first should recognize that ultrasonic NDE is a pervasive wave-based technology used to characterize materials and locate defects. Ultrasonic NDE techniques typically rely on the connections between elastic wave speeds in solids and the material properties or wave scattering from discontinuities as depicted in Fig. 1. *Ultrasonics* refers to sound waves, which in solids are elastic waves, having frequencies above the audible limit (~ 20 kHz). Ultrasonic NDE normally relies on linear features of the received signal such as velocity, amplitude, and attenuation. The descriptor *nonlinear* is employed to indicate that features of the received signal at frequencies other than the excitation frequency are analyzed. Ultrasonic energy is transferred from the excitation frequency to other frequencies due to material and geometric nonlinearities and discontinuities in the solid medium in which the waves are propagating. Nonlinear features of the received signal have a tendency to provide much-improved sensitivity to material degradation and defects relative to linear features, but they are much more difficult to measure because they are subtle. *Guided* waves are influenced, or physically guided, by the presence of boundaries or interfaces, which can limit propagation from 3D to 2D for a plate or to 1D for a rod. Important consequences of these boundaries are: generally longer propagation distances, dispersive pulse spreading, multiple modes having different wave speeds, and a complicated displacement profile (known as wavestructure) in the cross section of the waveguide. Advantages of NDE based on ultrasonic guided waves include volumetric inspection over relatively long distances or otherwise inaccessible components, while disadvantages include received signals that could be difficult to process due to the presence of multiple modes and complicated wave fields that may confound defect identification.

Metallic alloys remain the dominant type of structural material; therefore, NDE techniques and this Tutorial focus on them. One reason ultrasonic techniques typically work well in metals is that they have less internal damping than polymers and concrete (a composite having a variety of constituents and length scales). Moreover, metal structural elements such as pipes, shells, plates, rods, and rail are excellent waveguides.

The next sections describe how the potential of nonlinear ultrasonic guided waves for NDE applications is twofold—(1) to identify and track material degradation from a point early enough in the service life that there is time to make operational decisions and (2) to provide more reliable estimation of the damage state than is available by other NDE techniques.

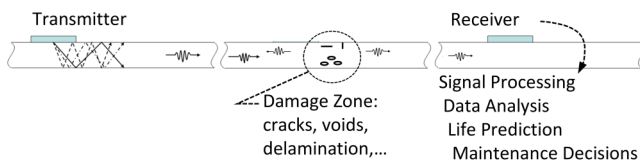


FIG. 1. Typical ultrasonic nondestructive evaluation (NDE) of a plate uses wave speed measurements to assess material degradation and wave scattering and attenuation to identify defects.

B. Early detection of degradation

Material degradation occurs under a variety of environmental and operational conditions. While brittle fracture is a sudden catastrophic mode of failure, there are many types of material degradation that occur over a much longer time scale:

- Fatigue—reduction in load-carrying capacity due to repeated or cyclic applied loads,
- Creep—deformation accumulated over time under a constant load (often thermally activated),
- Thermal aging—thermally activated phase changes that may affect the strength and fracture properties,
- Embrittlement (e.g., radiation and hydrogen)—formation of brittle inclusions that decrease the strength and fracture properties,
- Stress corrosion cracking—cracks form due to pitting corrosion induced stress concentrations under tensile stress.

Periodic NDE inspections and on-line monitoring provide a means to identify material degradation, to track its evolution over time, and to know when to repair or replace the component once it becomes unsafe. Thus, early detection of material degradation is a critical ability as illustrated in Fig. 2, which depicts the evolution of fatigue damage in a metal. A representative crack growth sequence from Kawagoishi *et al.*¹ is shown in Fig. 3. In generalized terms, crack sites nucleate due to the repetitious stress reversals, then crack precursors such as persistent slip bands develop and form microcracks that eventually link up, leading to a macrocrack that ultimately grows to its critical size causing fracture. The macrocrack detection threshold based on linear ultrasonics is qualitatively superimposed in Fig. 2. The threshold intersects the crack growth curve when there is but little remaining life, making it difficult or impossible to plan maintenance actions. Nonlinear ultrasonic measurements are able to detect precursors to the macroscale crack which could provide time for maintenance planning and logistics.

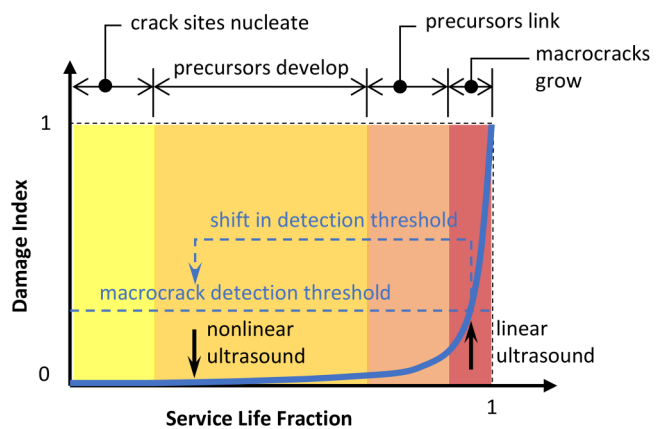
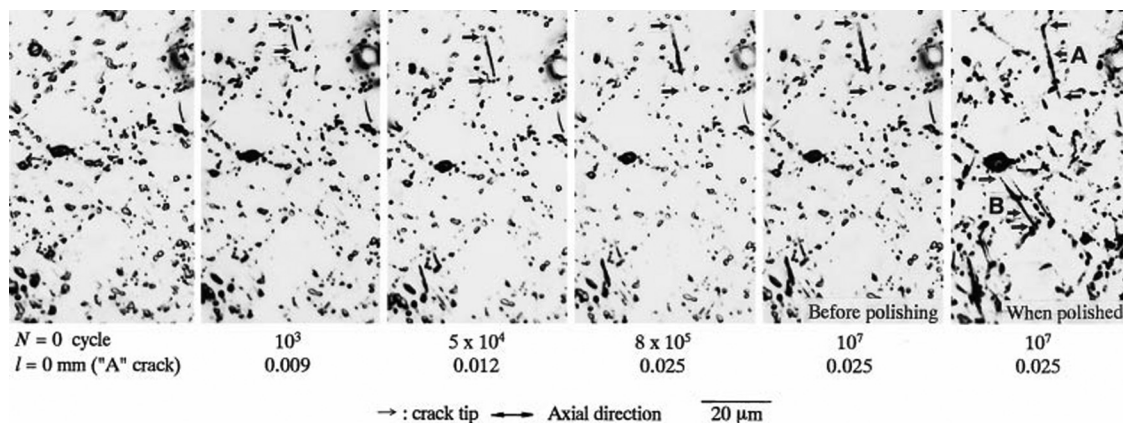


FIG. 2. Service life is limited by fatigue crack initiation and growth to a critical size as described by a damage index. Nonlinear ultrasonic methods can shift the detection of the damage process to much earlier in the service life.



How far nonlinear ultrasonic measurements shift the detection point to the left is an important and open question.

C. Strong sensitivity to early damage

Conventional linear ultrasonic methods can have a blind spot relative to closed cracks or kissing bonds, where the crack-like discontinuity is physically closed due to compressive stress. Figure 4, from Kawagoishi *et al.*,¹ shows a typical micrograph of a fatigue

crack in the nickel-based alloy Inconel 718 under tensile stress in one image and compressive stress in the other. The closure of the crack is apparent. The acoustic impedance mismatch due to the solid/air interface at an open crack or disbond causes wave scattering. But, if the interface is closed or partially closed, then the mismatch is reduced and less scattering occurs. However, if the tensile stresses associated with the elastic waves are sufficient to open a nominally closed crack, then there exists an asymmetry in the tensile/compression material behavior that generates nonlinearity.² Experimental results indicate that relative to linear ultrasonic parameters, nonlinear ultrasonic parameters provide earlier and more sensitive indication of fatigue damage.³

D. Sources of nonlinearity

Early nonlinear ultrasonics investigations focused on correlating the generation of higher harmonic bulk waves to the elastic nonlinearity and dislocations.^{4–6} The weak ultrasonic nonlinearity measured in experiments correlates with material nonlinearity associated with features of the microstructure, e.g., as shown by Hikata *et al.*,⁷ Cantrell,⁸ and Gao and Qu.⁹ It must be acknowledged that this is a difficult measurement to make and researchers have toiled monumentally to simplify the measurement and increase its sensitivity. The geometric nonlinearity associated with the nonlinear strain-displacement relation complicates the modeling, but measurement system nonlinearities are insidiously problematic. The discussion of system nonlinearities is postponed until Sec. VII so that we can focus on the material nonlinearities of interest until then. A good starting point is that all materials have anharmonicity associated with the crystal lattice related to the non-quadratic nature of the energy potential.^{8,10,11} This nonlinearity alone is generally not important for NDE, however it can be useful as a reference state. What is important for NDE is that dislocation structures, second phase particles, persistent slip bands, micro-cracks, etc. influence the material nonlinearity, and therefore their evolution can be detected through the ultrasonic nonlinearity. An example of the evolution of dislocation structures associated with

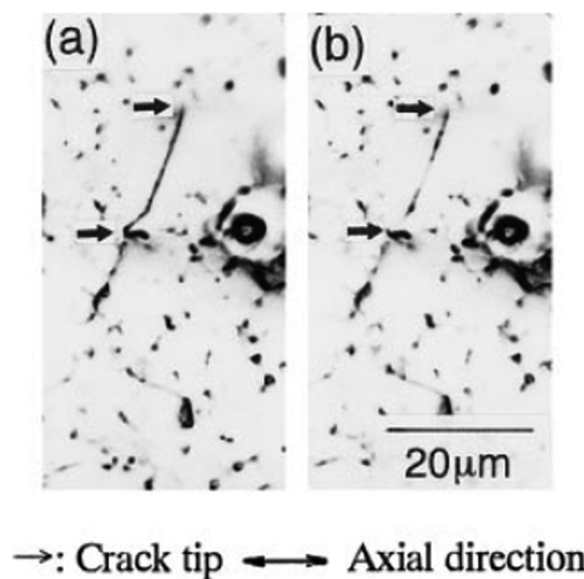


FIG. 4. (a) Crack opening under static tensile stress and (b) closure under static compressive stress. Reproduced with permission from Kawagoishi *et al.*, *Fatigue Fract. Eng. Mater. Struct.* **23**, 209 (2000). Copyright 2000 Blackwell Science Ltd.

plastic deformation in a martensitic stainless steel is given in Fig. 5, which is taken from Xiang *et al.*¹² There are numerous sources of information about nonlinear ultrasonics; books by Guyer and Johnson,¹³ Kundu,¹⁴ and Jhang *et al.*,¹⁵ chapters in books (e.g., by

Green,¹⁶ Norris,¹⁷ Cantrell,⁸ and Rose¹⁸), and review articles (e.g., Zheng *et al.*,¹⁹ Jhang,²⁰ Matlack,²¹ Chillara and Lissenden,²² and Li *et al.*²³), in addition to the research articles in journals, whose number has increased dramatically due to the high reward for the

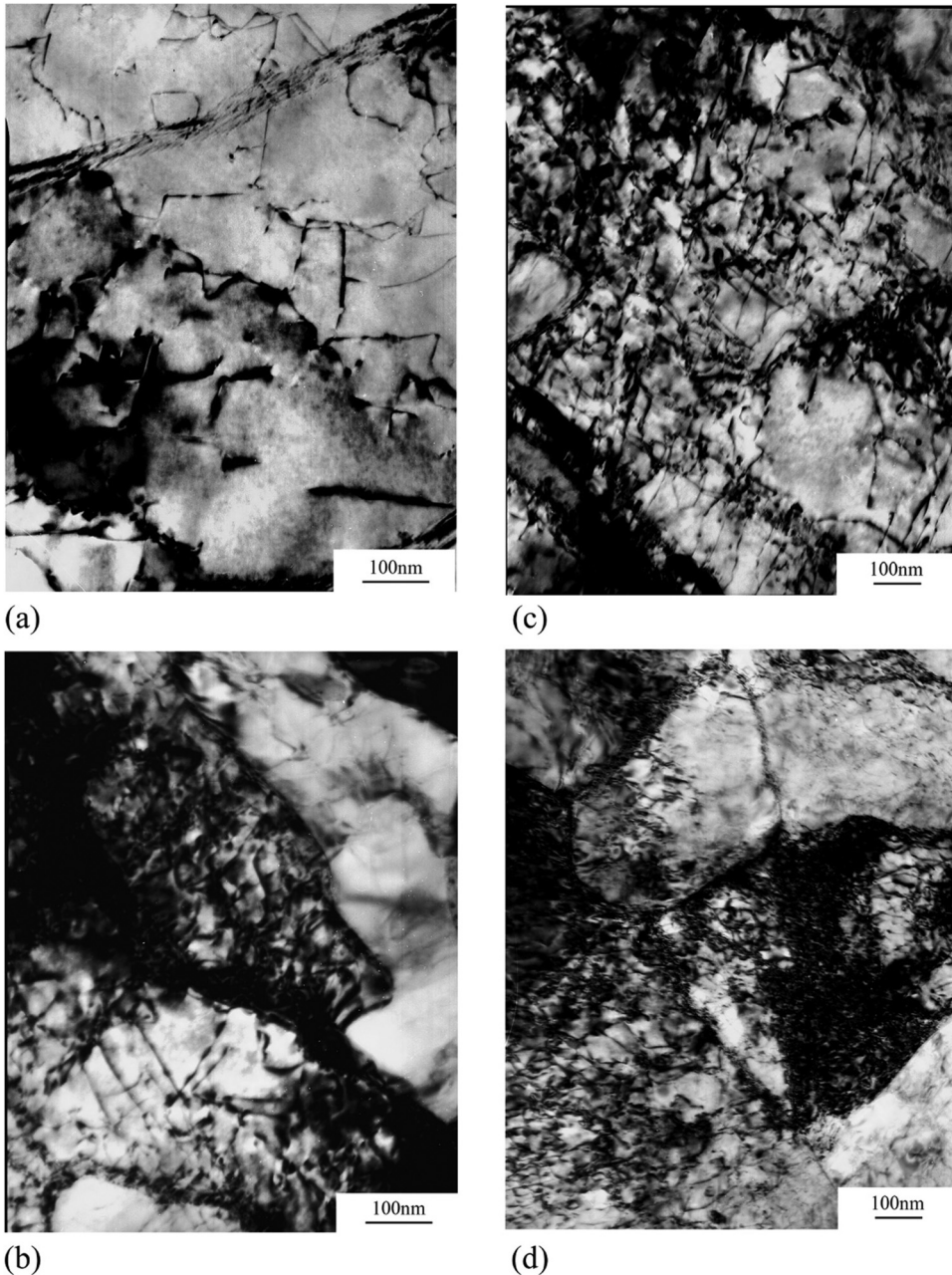


FIG. 5. Transmission electron microscope images of martensitic stainless steel: (a) undeformed with planar dislocation structures in the interior of lath martensite, DD = 0.35×10^{14} , (b) 1.14% plastic strain, DD = 1.30×10^{14} , (c) 1.73% plastic strain with homogeneously distributed and tangled dislocations, DD = 1.94×10^{14} , (d) 3.89% plastic strain with much denser and more tangled dislocations. Dislocation cell structures are observed for all deformation levels, with the thickest walls observed in (d). DD = dislocation density in m^{-2} . Reproduced with permission from Xiang *et al.*, J. Appl. Phys. 117, 214903 (2015). Copyright 2015 AIP Publishing LLC.

shift to earlier detection shown in Fig. 2. Readers may find research articles that focus on nonlinear ultrasonic guided waves helpful; thus, a very short list is provided here.^{24–29} Nonlinear ultrasonic guided waves have more recently emerged as a topic of significant interest and, therefore, comprise a relatively small portion of the whole of nonlinear ultrasonics, and an even smaller portion of nonlinear acoustics.

II. PHENOMENOLOGY OF ELASTIC WAVE DISTORTION

The phenomenology of elastic wave distortion responsible for nonlinear ultrasonics is described in this section at an introductory level. Although guided waves have multi-dimensional wave fields, here one-dimensional problems are analyzed as exemplars of the basic mathematics employed to describe higher harmonic generation and acoustoelasticity. Sandwiched between these two topics is an introduction to wave mixing.

A. Higher harmonic generation

A one-dimensional example (i.e., only one displacement component is nonzero) can help elucidate the distortion of waves propagating in a nonlinear elastic solid. Let the constitutive relation be given by a truncated Taylor series expansion in terms of the displacement gradient,

$$\sigma = E_o u' + \frac{1}{2} \beta E_o [u']^2, \quad (1)$$

where σ and u are the stress and displacement, E_o and β are linear elasticity and nonlinearity parameters, respectively, and $u' = \partial u / \partial x$ is the displacement gradient. The quadratic term in Eq. (1) causes the instantaneous stiffness to decrease in tension and increase in compression. In the absence of body forces, the balance of linear momentum is simply

$$\sigma' = \rho \ddot{u}, \quad (2)$$

where ρ is the mass density and $\ddot{u} = \partial^2 u / \partial t^2$. Substituting Eq. (1) into Eq. (2) and letting $c^2 = E_o / \rho$, the nonlinear wave equation becomes

$$\ddot{u} - c^2 u'' = \beta c^2 u' u''. \quad (3)$$

Letting $u = u_1 + u_2$ and assuming that $u_2 \ll u_1$ sets up use of a perturbation approach, where the derivatives of u_2 on the right-hand side of Eq. (3) are neglected, leading to the homogeneous (primary) solution

$$u_1 = A_1 \cos(kx - \omega t), \quad (4)$$

where k and ω are the wavenumber and the angular frequency of waves propagating in the x -direction. The trial function for the particular (secondary) solution of the nonhomogeneous partial differential equation of

$$u_2 = A_2 x \sin^2(kx - \omega t) \quad (5)$$

leads to the final solution

$$u(x, t) = A_1 \cos(kx - \omega t) + \frac{1}{8} \beta k^2 A_1^2 x [1 - \cos(2kx - 2\omega t)]. \quad (6)$$

The physical characteristics of this solution are that continuous primary waves (u_1) generate a quasi-static pulse of magnitude $\frac{1}{8} \beta k^2 A_1^2 x$ and second harmonics (at frequency 2ω) having cumulative amplitude $\frac{1}{8} \beta k^2 A_1^2 x$. Since the second harmonics have wave-number $2k$, they propagate at the same velocity as the primary waves; i.e., $c = \omega/k = 2\omega/2k$. If the Taylor series in Eq. (1) were not truncated at order 2, then harmonics of order 3 and above would also exist in the solution.

The solution in Eq. (6) has important limitations; i.e., it applies to planar continuous waves in a lossless media having $u_2 \ll u_1$. A result of the perturbation solution is that while the amplitude of the primary waves is constant, the amplitude of the secondary waves increases with propagation distance. This artifact of the perturbation solution suggests that energy is created, which of course is physically unrealistic. The amplitude of the primary waves must decrease in accordance with the power that flows to the secondary waves. The perturbation solution relies on this being inconsequential, which is a point that we will return to in Sec. VIII B. The fact that the primary and secondary waves have the same phase velocity means that they are synchronized or in-phase, which has important consequences on their interaction as well as their reception. Figure 6 illustrates how a material acts like a nonlinear operator, and through self-interaction an input signal is distorted. By transforming the temporal signal into the frequency domain with a Fourier transform or fast Fourier transform (FFT), the higher harmonics at integer multiples of the input frequency f_0 (where $\omega = 2\pi f$) are apparent. The cumulative nature of the secondary waves is illustrated in Fig. 7. Note that the amplitude of the distorted primary waves increases slightly with propagation distance and that due to the fundamental relationship between frequency, velocity, and wavelength ($c_p = \lambda f$), the wavelength of the higher harmonics must decrease in accordance with the increase in frequency since the velocities are equal.

B. Wave mixing

Instead of analyzing monochromatic waves as above, we could be interested in wave mixing and analyze continuous waves having two distinct frequencies f_a and f_b . In the linearized case of infinitesimal displacements in a linear elastic solid, the principle of superposition applies, and the waves do not mix. However, if the displacements are finite or the material is nonlinear, then mutual interactions will occur, and the superposition principle does not apply. The mutual interactions cause energy transfer to different frequencies; i.e., primary waves at f_a and f_b generate second order waves at $|f_a \pm f_b|$, third order waves at $|2f_a \pm f_b|$ and $|f_a \pm 2f_b|$, and so forth. Second order mutual interactions from wave mixing are shown in Fig. 6(b). Clearly, second harmonic generation and the quasi-static pulse are second order manifestations of wave mixing when $f_a = f_b$ and thus can be thought of as due to self-interaction; second harmonics are generated at the sum frequency and the quasi-static pulse occurs at the difference frequency.

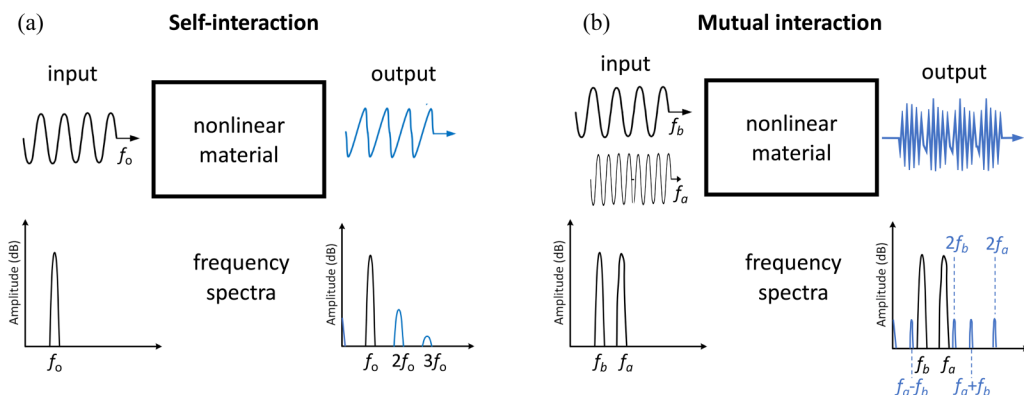


FIG. 6. Material as a nonlinear operator for (a) self-interaction of sinusoidal waves at frequency f_o and (b) mutual interaction of sinusoidal waves at frequencies f_a and f_b . Nonlinear material distorts the waves and generates harmonics.

In wave mixing problems, the interaction angle between the primary wave fields a and b is θ , with waves a being in the X_1 -direction. Wave interactions are classified as co-directional ($\theta = 0^\circ$), counter-propagating ($\theta = 180^\circ$), and non-collinear ($\theta \neq 0^\circ$ and $\theta \neq 180^\circ$). The angle γ defines the wavevector direction of the secondary wave field with respect to waves a .

C. Acoustoelasticity

Material nonlinearity leads to the elastic wave speed being dependent upon stress in a second order fashion, which is known as acoustoelasticity. There are many good sources for acoustoelasticity, including Green,¹⁶ Pau *et al.*,³⁰ Norris,¹⁷ and Guyer and Johnson.¹³ The treatment here is rudimentary. Once again,

consider a one-dimensional displacement problem to uncover the basic physics in a simplistic fashion. Setting $\beta = 0$ in Eq. (3), c is interpreted as the wave speed, which is constant for a linear elastic material. Now return to Eq. (3), but with $\beta \neq 0$ this time. Let the strain be a combination of a homogeneous and constant static displacement gradient, u'_s , and a much smaller dynamic displacement gradient, u'_d , associated with an elastic wave. The stress given by Eq. (1) is

$$\sigma = [E_o u'_s] + \left[E_o u'_d + \frac{1}{2} E_o \beta 2u'_s u'_d \right] + \dots, \quad (7)$$

where on the right-hand-side the first bracketed term is the static component, σ_s , the second bracketed term is the dynamic stress, σ_d , and the other terms not written out are higher order terms to be neglected. The balance of linear momentum [Eq. (2)] is written in terms of the dynamic stress,

$$\rho \ddot{u} = \sigma'_d = E_o [1 + \beta u'_s] u''_d, \quad (8)$$

from which the wave speed is interpreted to be

$$c^2 = \frac{E_o [1 + \beta u'_s]}{\rho}, \quad (9)$$

where the static component of the displacement gradient, u'_s , in turn depends on the static stress since $\sigma_s = E_o u'_s$. E_o can be given in terms of Young's modulus and Poisson's ratio in this confined 1D problem. When determined in terms of the Landau-Lifshitz third order elastic constants β is negative (approximately -15 for aluminum) (from Guyer and Johnson,¹³ Sec. 3.3, $\beta = 3 + 3[2A + 6B + 2C]/[3K + 4\mu]$, where K and μ and A , B , C are the bulk modulus, shear modulus, and third order constants, respectively), thus relative to zero static stress, the wave speed increases for a compressive stress and decreases for a tensile stress.

Guided wave acoustoelasticity can be applied to various problems of practical interest; including, for example: thermally activated

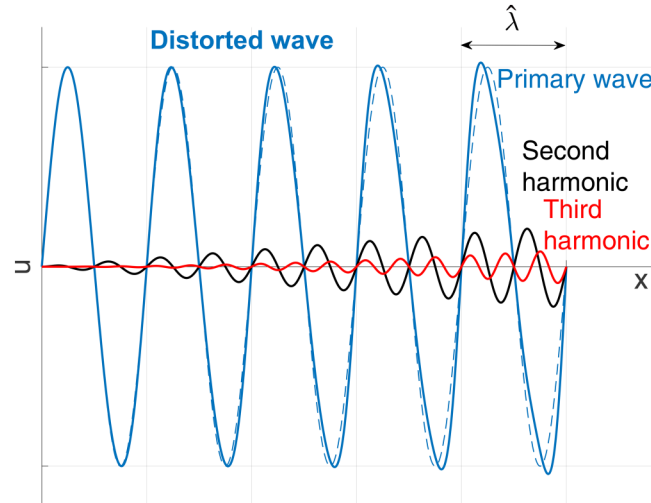


FIG. 7. Nonlinear wave propagation exhibits distortion of the primary waves due to the generation of cumulative higher harmonics.

buckling of restrained rail by Nucera and Lanza di Scalea,^{11,31} measurement of prestress in multi-strand cable by Dubuc *et al.*,³² and measurement of applied stress, residual stress, and prestress in plates.^{33–36} However, in order to limit the scope of the Tutorial, guided wave acoustoelasticity will not be considered further.

III. LINEAR CHARACTERISTICS OF ULTRASONIC GUIDED WAVES

In this section, a linear elastic analysis of ultrasonic guided waves is provided, which will serve as a starting point for the more complex problem of nonlinear guided waves. The characteristics of guided waves are analyzed by forcing the governing differential equations to satisfy the boundary conditions. Starting with the balance of linear momentum in the absence of body forces for a linear elastic material having infinitesimal strains we have

$$\nabla \cdot \boldsymbol{\sigma} = \rho \ddot{\mathbf{u}}, \quad (10)$$

$$\boldsymbol{\sigma} = \mathbf{C} \boldsymbol{\epsilon}, \quad (11)$$

$$\boldsymbol{\epsilon} = \frac{1}{2} [\nabla \mathbf{u} + (\nabla \mathbf{u})^T], \quad (12)$$

where \mathbf{u} is the displacement vector and $\boldsymbol{\sigma}$, $\boldsymbol{\epsilon}$, and \mathbf{C} are the stress, strain, and elastic stiffness tensors, respectively. Combining Eqs. (10)–(12) for the special case of a homogeneous isotropic material gives the wave equation

$$\mu \nabla^2 \mathbf{u} + [\lambda + \mu] \nabla \nabla \cdot \mathbf{u} = \rho \ddot{\mathbf{u}}, \quad (13)$$

where λ and μ are Lame's constants. Considering a homogeneous waveguide having a traction-free lateral boundary, free wave propagation is given by the solution of the hyperbolic differential equation [Eq. (13)] with Neumann boundary conditions. Common applications include plates, hollow cylinders, and rail sections as shown in Fig. 8. For free wave propagation, seek solutions of the form

$$\mathbf{u}(\mathbf{x}, t) = \mathbf{U}(\mathbf{x}) e^{i[kx_1 - \omega t]} \quad (14)$$

for a wave vector in the x_1 direction, where $i = \sqrt{-1}$. Substituting Eq. (14) into Eq. (13) and then applying the Neumann boundary conditions results in an eigenproblem. Given angular frequency ω , the eigenvalue is the wavenumber k and the eigenvector is $\mathbf{U}(\mathbf{x})$,

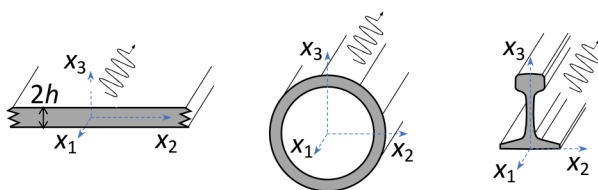


FIG. 8. Cross sections of some common waveguides: plate, hollow cylinder, rail.

which is known as the wavestructure (akin to a mode shape in steady state vibration). The wavestructure is in general three-dimensional, although there are special cases where the displacement components are decoupled. Analytical solutions are only available for the special case of shear-horizontal (SH) waves in a plate, thus numerical techniques are used. Initially, the transfer matrix method and global matrix method were used to obtain solutions, but now a semi-analytical finite element (SAFE) methodology is more common, as described by Rose.³⁷ Briefly, the SAFE method presumes a harmonic wavefield in the axial direction of the waveguide (x_1 in Fig. 8). Thus, the problem is reduced to solving the wave equation subject to the traction-free boundary conditions on the lateral surface by discretizing the waveguide's cross section. The result is a quadratic eigenproblem having eigenvalues and eigenvectors that are the wavenumbers and wavestructures, respectively, at a prescribed frequency.

While Eq. (13) does not apply to anisotropic waveguides, the dispersion curves for anisotropic waveguides are obtained in an analogous manner, i.e., substitute Eq. (14) into Eqs. (10)–(12) and solve the hyperbolic differential equation subject to the Neumann boundary conditions. The SAFE methodology is commonly used for this purpose, although the partial wave method discussed below is an alternative. Dispersion curves for layered media require that continuity conditions for the displacements and surface tractions be satisfied at the interfaces between layers in addition to the Neumann boundary conditions on the lateral boundary.

The following subsections highlight specific information about guided wave propagation in plates, hollow cylinders, and waveguides of arbitrary cross section.

A. Plates

Given the plate waveguide shown in Fig. 8, if it is isotropic, then the wave types decouple into Lamb waves polarized in the sagittal plane (x_1 - x_3 plane) and SH waves polarized in the x_2 direction. The dispersion relation obtained by substituting Eq. (14) into Eq. (13) and then applying the traction-free boundary conditions at $x_3 = \pm h$ is a transcendental equation

$$\frac{\tan(qh)}{\tan(ph)} = - \left[\frac{4k^2 pq}{[q^2 - k^2]^2} \right]^{\pm 1} \quad (15)$$

for Lamb waves, where on the right-hand side the exponent +1 is for symmetric wave modes and -1 is for antisymmetric wave modes. Symmetry and antisymmetry are defined by the u_1 displacement component. Furthermore, $p^2 = k_L^2 - k^2$ and $q^2 = k_T^2 - k^2$, where subscripts L and T refer to longitudinal and transverse (shear) bulk waves, and the fundamental relationship between wavenumber, phase velocity, and angular frequency applies, i.e., $c_p = \omega/k$. For SH waves, the dispersion relation is simply

$$\begin{aligned} \sin(qh) &= 0 && \text{for symmetric modes (when } u_2 \text{ is symmetric),} \\ \cos(qh) &= 0 && \text{for antisymmetric modes (when } u_2 \text{ is antisymmetric).} \end{aligned} \quad (16)$$

Sometimes, it is useful to interpret Lamb waves and guided waves in anisotropic plates as a superposition of bulk waves. These bulk

waves may have a real-valued k_3 , in which case they reflect off the top and bottom surfaces of the plate; or they may have an imaginary-valued k_3 , in which case they propagate along the surface of the plate. The so-called partial waves method of Solie and Auld³⁸ uses a superposition of all possible bulk waves to satisfy the boundary conditions and determine the dispersion relations.³⁹

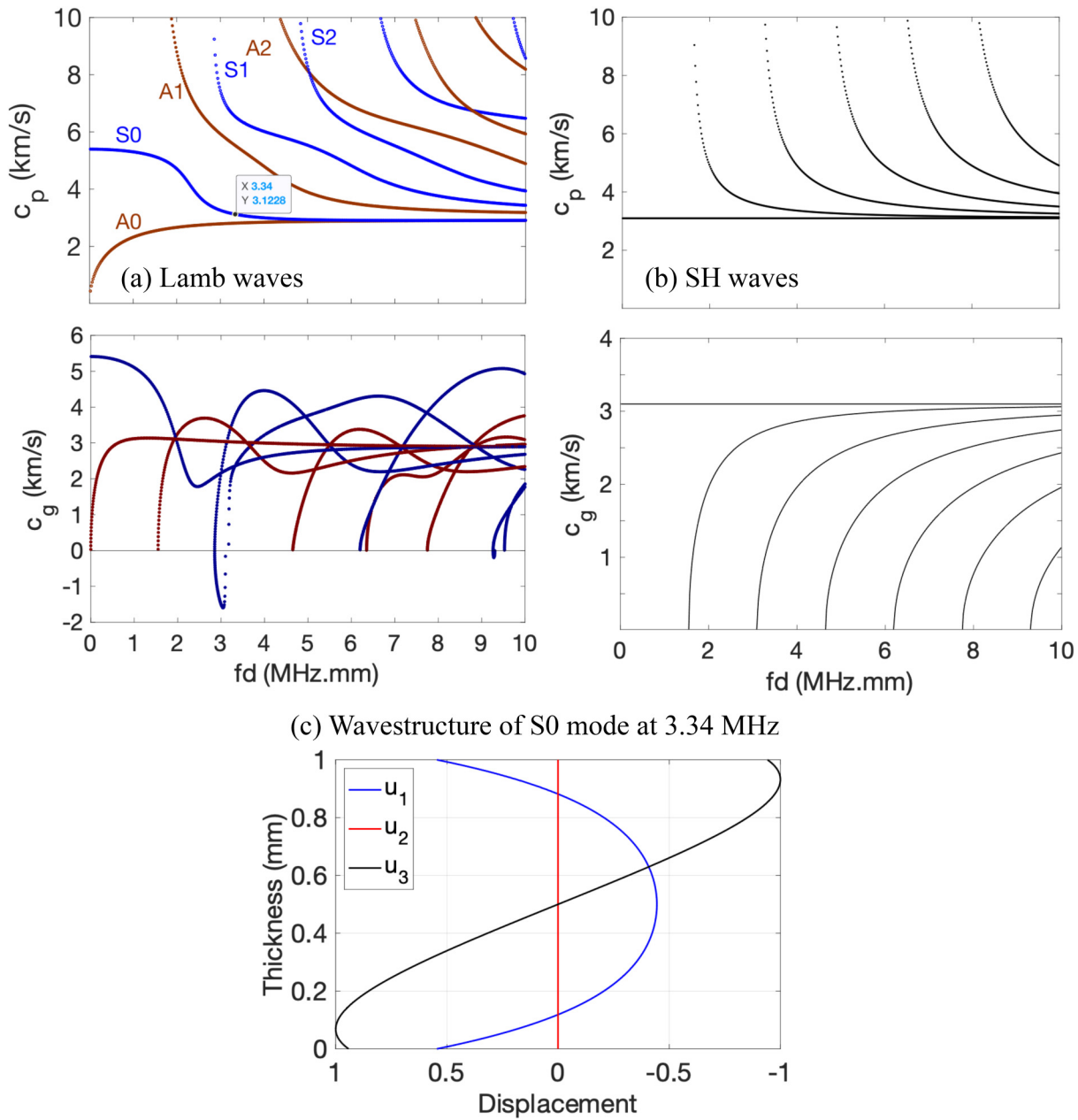


FIG. 9. Phase and group velocity dispersion curves for an aluminum plate: (a) Lamb waves*, (b) SH waves, and (c) wavestructure of the S_0 Lamb wave mode at 3.34 MHz. $c_L = 6.35$ km/s and $c_T = 3.10$ km/s. *Reproduced with permission from Hakoda and Lissenden, J. Sound Vib. **469**, 115165 (2020) Copyright 2020 Elsevier.

wavenumbers and not the evanescent modes associated with imaginary and complex wavenumbers. However, the evanescent modes are important for modal expansions. The group velocity is the speed at which a wave packet travels; it describes the energy velocity. Thus, group velocity is important for nonlinear guided waves in that energy transfer from primary waves to secondary waves can only occur when the wave packets overlap, which is dictated by their group velocities. Moreover, the synchronism or phase matching condition introduced in Sec. II A is often assessed for guided waves in terms of the phase velocity.

B. Hollow cylinders

Pipes and tubing are hollow cylinders (see Fig. 8) that act as excellent waveguides that permit the ultrasonic energy to propagate long distances. It is more convenient to analyze hollow cylinders in a cylindrical (r, θ, z) coordinate system, for which details are provided by Rose.³⁷ Three classes of guided waves are defined. Longitudinal (L) modes have r and z particle displacement component profiles in the r direction, torsional (T) modes have θ particle displacement profiles in the r direction. Both longitudinal and torsional modes are axisymmetric and denoted L(0,n) and T(0,n) where n is a whole number defining the wave mode. These should not be confused with L and T bulk waves. The third class of guided waves is not axisymmetric and is termed flexural modes; and is characterized by circumferential orders m, in addition to wave modes n. Flexural waves are denoted L(m,n) or T(m,n) depending on their polarization. The longitudinal and torsional modes are in fact zeroth circumferential order flexural modes. The phase velocity dispersion curves for a hollow cylinder are shown in Fig. 10.⁴¹ Note the similarity between the L(0,n) and T(0,n) modes in a hollow cylinder and the Lamb and SH modes in a plate. One can imagine making a longitudinal cut in the cylinder and then unwrapping the cylinder to form a plate, but of course this ignores the effect of curvature.

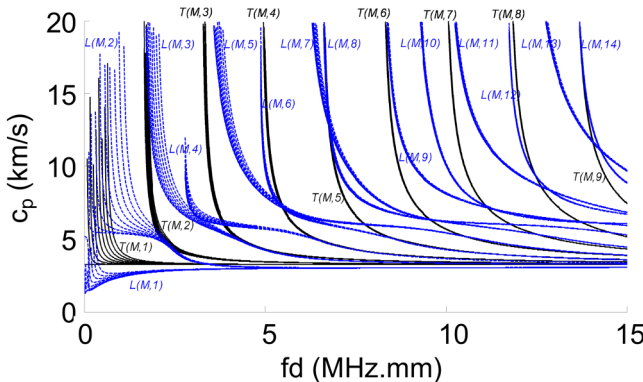


FIG. 10. Phase velocity dispersion curves for a steel pipe having an inner radius of 9 mm. $c_L = 5.96$ km/s and $c_T = 3.23$ km/s. Reproduced with permission from Liu *et al.*, J. Appl. Phys. **115**, 214901 (2014). Copyright 2014 AIP Publishing LLC.

C. Arbitrary cross section

Plate and hollow cylinder cross sections are geometrically simple enough that they can be solved without discretization, but discretizing a cross section enables application of the SAFE method to determine the dispersion curves. The method is termed semi-analytical because it presumes the wave propagation to be harmonic and thus discretization is limited to the cross section of the waveguide. The rail shown in Fig. 8 is a good example of what is meant by an arbitrary cross section. The phase velocity and group velocity dispersion curves obtained by Hakoda and Lissenden⁴⁰ are shown in Fig. 11. Clearly, the dispersion curves for rail have a high density of propagating modes even for the smaller frequency range shown in Fig. 11. The wavestuctures are three dimensional and indispensable for assessing the displacement, strain, and stress distributions within the cross section.

D. Half-space

Rayleigh waves propagate along the surface of a traction-free homogeneous isotropic half-space. Most of the energy of a Rayleigh

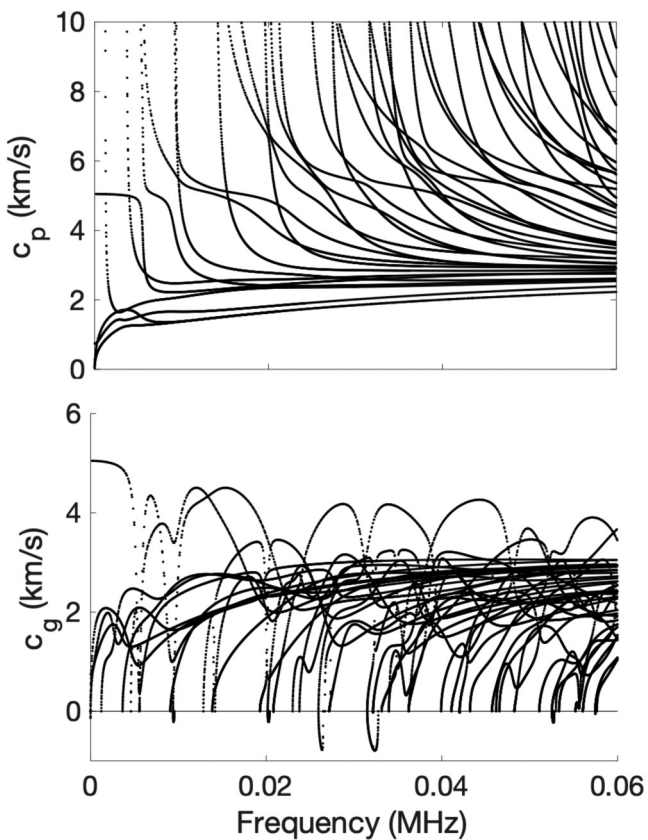


FIG. 11. Phase velocity and group velocity dispersion curves for a 136RE steel rail section. Reproduced with permission from Hakoda and Lissenden, J. Sound Vib. **469**, 115165 (2020). Copyright 2020 Elsevier.

wave is within one wavelength of the free surface. Elliptical particle motion is characteristic of Rayleigh waves and the phase velocity is obtained as the real root of a cubic polynomial derived from the wave equation. Rayleigh waves are nondispersive. Quasi-Rayleigh waves propagate in a plate of finite thickness rather than a half-space. They occur where the A₀ and S₀ fundamental Lamb wave dispersion curves converge.

IV. MODELING NONLINEARITY

Having highlighted the key features of ultrasonic guided waves in the previous section, we now turn our attention to modeling the ultrasonic nonlinearity. The weak ultrasonic nonlinearity is rooted in the material and geometric nonlinearities associated with finite amplitude waves. Continuum mechanics provides the necessary framework for the formulation of the field equations in Sec. IV A. Analysis of the nonlinearity associated with discontinuities such as cracks, disbonds, and delaminations is summarized in Sec. IV B. It is convenient to combine the nonlinearities into driving forces that can be used within a perturbation analysis. The approach in Sec. IV C entails decomposing the displacement field into its primary and secondary components and formally defining boundary value problems that can be solved by assuming that the secondary wave field is small compared to the primary wave field, which is reasonable because the primary and secondary wave amplitudes often vary by two orders of magnitude or more. The solution to the nonhomogeneous differential equations is carried out in Sec. IV D using a normal mode expansion based on an orthogonality relation obtained from reciprocity.

A. Field equations

To formulate the field equations for nonlinear guided waves, we use a Lagrangian description and consider the current configuration to be described by coordinates x_i and the material configuration to be described by coordinates X_i as shown in Fig. 12. As detailed in texts on continuum mechanics (e.g., Malvern⁴²), the displacement vector is $\mathbf{u} = \mathbf{x} - \mathbf{X}$ and the current and material

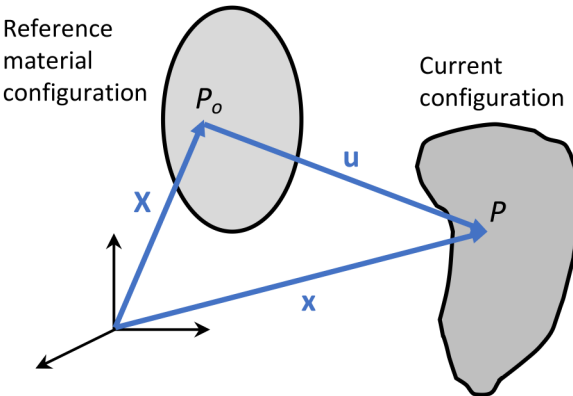


FIG. 12. Material and current configurations.

coordinates are connected through the deformation gradient tensor

$$\mathbf{F} = \frac{\partial \mathbf{x}}{\partial \mathbf{X}} = \mathbf{I} + \frac{\partial \mathbf{u}}{\partial \mathbf{X}} = \mathbf{I} + \mathbf{H}, \quad (17)$$

where \mathbf{I} is the identity tensor of rank 2 and \mathbf{H} is the displacement gradient. Conservation of mass is enforced by setting $\rho dV = \rho_o dV_o$, where dV and dV_o are infinitesimal volume elements in the current and material coordinate systems, respectively. Thus, $\rho \det(\mathbf{F}) = \rho_o$.

Using a hyperelastic material model, which posits the existence of an elastic potential function, W , the second Piola-Kirchhoff stress tensor is given by

$$\mathbf{T}_{PK2} = \frac{\partial W}{\partial \mathbf{E}}, \quad (18)$$

where \mathbf{E} is the Lagrangian strain tensor. By the elastic potential function's dependence on the Lagrangian strain, $W(\mathbf{E})$, we interpret W as the strain energy per unit undeformed volume. This formulation uses both Piola-Kirchhoff stresses to properly account for finite (large) strain, and it is important to distinguish them from the Cauchy stress. While the Cauchy stress, σ , is defined with respect to the current configuration, the Piola-Kirchhoff stresses are defined with respect to the material configuration. The first Piola-Kirchhoff stress tensor relates force in the current configuration with area in the material configuration, while the second Piola-Kirchhoff stress tensor relates force in the material configuration with area in the material configuration,

$$\mathbf{T}_{PK1} = \mathbf{T}_{PK2} \cdot \mathbf{F}^T, \quad (19)$$

$$\mathbf{T}_{PK1} = \det(\mathbf{F}) \mathbf{F}^{-1} \cdot \sigma, \quad (20)$$

$$\mathbf{T}_{PK2} = \det(\mathbf{F}) \mathbf{F}^{-1} \cdot \sigma \cdot [\mathbf{F}^{-1}]^T. \quad (21)$$

$\mathbf{S} = \mathbf{T}_{PK1}$ is a two-point tensor that is not in-general symmetric and is the energy conjugate to \mathbf{F} , while \mathbf{T}_{PK2} is a one-point tensor that is symmetric.

Landau and Lifshitz¹⁰ expanded the elastic potential function in terms of strain for homogeneous isotropic solid media,

$$W = \frac{\lambda}{2} [\text{tr}(\mathbf{E})]^2 + \mu \text{tr}(\mathbf{E}^2) + \frac{A}{3} \text{tr}(\mathbf{E}^3) + B \text{tr}(\mathbf{E}) \text{tr}(\mathbf{E}^2) + \frac{C}{3} [\text{tr}(\mathbf{E})]^3 + O(\mathbf{E}^4), \quad (22)$$

where $\text{tr}(\cdot)$ denotes the trace, λ and μ are Lame's constants and A , B , and C are Landau and Lifshitz's third order elastic constants, which are directly related to Murnaghan's third order elastic constants l , m , and n as given by Norris.¹⁷ Higher order terms in the series must be kept in order to analyze higher harmonics; e.g., Liu *et al.*⁴³ used a fourth order elastic potential function. The strain energy function must include third order terms to model generation of second order harmonics from self-interaction or mutual

interaction; it must include fourth order terms to give a consistent representation of third order harmonics, and so on.

The elastic potential function for homogeneous anisotropic solid media requires more constants. For a transversely isotropic material, Zhao *et al.*⁴⁴ expanded the elastic potential function to third order in terms of the five strain invariants after Spencer,⁴⁵

$$\begin{aligned} W &= W(tr\mathbf{E}, tr\mathbf{E}^2, tr\mathbf{E}^3, \mathbf{a} \cdot \mathbf{Ea}, \mathbf{a} \cdot \mathbf{E}^2\mathbf{a}), \\ W &= \alpha_1[tr\mathbf{E}]^2 + \alpha_2[tr\mathbf{E}][\mathbf{a} \cdot \mathbf{Ea}] + \alpha_3[tr\mathbf{E}^2] + \alpha_4[\mathbf{a} \cdot \mathbf{Ea}]^2 + \alpha_5[\mathbf{a} \cdot \mathbf{E}^2\mathbf{a}] \\ &\quad + \beta_1[tr\mathbf{E}]^3 + \beta_2[tr\mathbf{E}][tr\mathbf{E}^2] + \beta_3[tr\mathbf{E}][\mathbf{a} \cdot \mathbf{Ea}]^2 + \beta_4[tr\mathbf{E}][\mathbf{a} \cdot \mathbf{E}^2\mathbf{a}] \\ &\quad + \beta_5[tr\mathbf{E}]^2[\mathbf{a} \cdot \mathbf{Ea}] + \beta_6[tr\mathbf{E}^2][\mathbf{a} \cdot \mathbf{Ea}] + \beta_7[tr\mathbf{E}^3] + \beta_8[\mathbf{a} \cdot \mathbf{Ea}]^3 \\ &\quad + \beta_9[\mathbf{a} \cdot \mathbf{Ea}][\mathbf{a} \cdot \mathbf{E}^2\mathbf{a}] + O(\mathbf{E}^4), \end{aligned} \quad (23)$$

where α_i ($i = 1, \dots, 5$) are the coefficients of the quadratic terms that correspond to linear elastic material behavior, and β_i ($i = 1, \dots, 9$) are the coefficients of the cubic terms that correspond to nonlinear elastic material behavior. See also Rauter and Lammering.⁴⁶

The Lagrangian strain tensor is related to the displacement gradient through

$$\mathbf{E} = \frac{1}{2}[\mathbf{H} + \mathbf{H}^T + \mathbf{H}^T\mathbf{H}], \quad (24)$$

where the $\mathbf{H}^T\mathbf{H}$ term is a geometric nonlinearity. Consider now the displacement fields, actually let us consider the displacement gradient fields, between two interacting elastic waves a and b . Start by decomposing the total displacement gradient into parts associated with the primary waves a and b (\mathbf{H}_a and \mathbf{H}_b), the self-interactions of waves a and b (\mathbf{H}_{aa} and \mathbf{H}_{bb}), and the mutual interactions of waves a and b (\mathbf{H}_{ab}),

$$\mathbf{H} = \mathbf{H}_a + \mathbf{H}_b + \mathbf{H}_{aa} + \mathbf{H}_{bb} + \mathbf{H}_{ab} + \dots, \quad (25)$$

where only the terms for up to second order interactions are written explicitly. Likewise, the first Piola-Kirchhoff stress can be decomposed in terms of these quantities and then further decomposed into the linear and nonlinear parts from each of these terms,

$$\begin{aligned} \mathbf{S}(\mathbf{H}) &= \mathbf{S}_L(\mathbf{H}_a) + \mathbf{S}_L(\mathbf{H}_b) + \mathbf{S}_L(\mathbf{H}_{aa}) + \mathbf{S}_L(\mathbf{H}_{bb}) + \mathbf{S}_L(\mathbf{H}_{ab}) \\ &\quad + \mathbf{S}_{NL}(\mathbf{H}_a + \mathbf{H}_b), \end{aligned} \quad (26)$$

where the nonlinear interaction can be written as

$$\begin{aligned} \mathbf{S}_{NL}(\mathbf{H}_a + \mathbf{H}_b) &= \mathbf{S}_{NL}(\mathbf{H}_a, \mathbf{H}_a, 2) + \mathbf{S}_{NL}(\mathbf{H}_b, \mathbf{H}_b, 2) \\ &\quad + \mathbf{S}_{NL}(\mathbf{H}_a, \mathbf{H}_b, 2), \end{aligned} \quad (27)$$

and the term $\mathbf{S}_{NL}(\mathbf{H}_a, \mathbf{H}_b, 2)$ can be interpreted to mean the interactions of order 2 between \mathbf{H}_a and \mathbf{H}_b . The other two terms represent the second order self-interactions. The actual terms that comprise the right-hand side of Eq. (27) are lengthy but obtained in a straightforward manner by substituting the elastic potential function, Eq. (22) for an isotropic material, into Eqs. (18) and (19).

Doing so for mutual interactions gives

$$\begin{aligned} \mathbf{S}_{NL}(\mathbf{H}_a, \mathbf{H}_b, 2) &= \frac{\lambda}{2}\text{tr}(\mathbf{H}_b + \mathbf{H}_b^T)\mathbf{H}_a + \mu\mathbf{H}_a[\mathbf{H}_b + \mathbf{H}_b^T] \\ &\quad + \frac{\lambda}{2}\text{tr}(\mathbf{H}_a + \mathbf{H}_a^T)\mathbf{H}_b + \mu\mathbf{H}_b[\mathbf{H}_a + \mathbf{H}_a^T] \\ &\quad + \frac{\lambda}{2}\text{tr}(\mathbf{H}_a^T\mathbf{H}_b + \mathbf{H}_b^T\mathbf{H}_a)\mathbf{I} + 2C\text{tr}(\mathbf{H}_a)\text{tr}(\mathbf{H}_b)\mathbf{I} \\ &\quad + \mu[\mathbf{H}_a^T\mathbf{H}_b + \mathbf{H}_b^T\mathbf{H}_a] + B\text{tr}(\mathbf{H}_a)[\mathbf{H}_b + \mathbf{H}_b^T] \\ &\quad + B\text{tr}(\mathbf{H}_b)[\mathbf{H}_a + \mathbf{H}_a^T] + \frac{B}{2}\text{tr}(\mathbf{H}_a\mathbf{H}_b + \mathbf{H}_b\mathbf{H}_a) \\ &\quad + \mathbf{H}_a^T\mathbf{H}_b + \mathbf{H}_b^T\mathbf{H}_a)\mathbf{I} + \frac{A}{4}[\mathbf{H}_a\mathbf{H}_b + \mathbf{H}_b\mathbf{H}_a + \mathbf{H}_a^T\mathbf{H}_b^T \\ &\quad + \mathbf{H}_b^T\mathbf{H}_a^T + \mathbf{H}_a^T\mathbf{H}_b + \mathbf{H}_b^T\mathbf{H}_a + \mathbf{H}_a\mathbf{H}_b^T + \mathbf{H}_b\mathbf{H}_a^T]. \end{aligned} \quad (28)$$

Analogous equations can be written for the nonlinear stress terms due to self-interaction of waves a and also the self-interaction of waves b .

The conservation of linear momentum gives the equation of motion, in the absence of body forces, to be

$$\nabla \cdot \mathbf{S}(\mathbf{H}) = \rho \ddot{\mathbf{u}}, \quad (29)$$

which is solved subject to the boundary conditions. If we consider the plate problem shown in Fig. 8, the Neumann boundary conditions are

$$\mathbf{S}(\mathbf{H}) \cdot \mathbf{n} = 0 \text{ for } X_3 = \pm h. \quad (30)$$

Equations (29) and (30) represent the boundary value problem for free wave propagation in a plate, whose solution is given in Sec. IV C.

B. Discontinuities

Although a diversion from the principal subject matter based on material nonlinearity, there exists a class of problems for which nonlinear guided waves carry information about a single discontinuity in the structure. The existence of a delamination, crack, or interface that is closed or partially closed is notoriously difficult to detect with conventional linear ultrasonic methods. However, the opening and closing of the delamination, crack, or interface associated with the tensile and compressive portions of a wave give rise to a contact acoustic nonlinearity (CAN), which can be leveraged for nondestructive detection and characterization. The CAN is generally associated with the asymmetric response due to the “clapping” of the crack faces and friction, which generates higher harmonics and subharmonics. The literature on the CAN is itself quite voluminous, of which only a few are cited herein.^{2,47–49}

C. Boundary value problems in plates

Due to the weak nonlinearity ($\mathbf{u}_{aa}, \mathbf{u}_{bb}, \mathbf{u}_{ab} \ll \mathbf{u}_a, \mathbf{u}_b$) in the ultrasonic guided waves problem, a perturbation method based

on successive approximations can be employed to reorganize Eqs. (29) and (30) into five separate boundary value problems,

$$\nabla \cdot (\mathbf{S}_L(\mathbf{H}_a)) - \rho \ddot{\mathbf{u}}_a = 0, \quad (31)$$

$$\mathbf{S}_L(\mathbf{H}_a) \cdot \mathbf{n} = 0 \text{ for } X_3 = \pm h,$$

$$\nabla \cdot (\mathbf{S}_L(\mathbf{H}_b)) - \rho \ddot{\mathbf{u}}_b = 0, \quad (32)$$

$$\mathbf{S}_L(\mathbf{H}_b) \cdot \mathbf{n} = 0 \text{ for } X_3 = \pm h,$$

$$\nabla \cdot (\mathbf{S}_L(\mathbf{H}_{aa})) - \rho \ddot{\mathbf{u}}_{aa} = -\nabla \cdot (\mathbf{S}_{NL}(\mathbf{H}_a, \mathbf{H}_a, 2)), \quad (33)$$

$$\mathbf{S}_L(\mathbf{H}_{aa}) \cdot \mathbf{n} = -\mathbf{S}_{NL}(\mathbf{H}_a, \mathbf{H}_a, 2) \cdot \mathbf{n} \text{ for } X_3 = \pm h,$$

$$\nabla \cdot (\mathbf{S}_L(\mathbf{H}_{bb})) - \rho \ddot{\mathbf{u}}_{bb} = -\nabla \cdot (\mathbf{S}_{NL}(\mathbf{H}_b, \mathbf{H}_b, 2)), \quad (34)$$

$$\mathbf{S}_L(\mathbf{H}_{bb}) \cdot \mathbf{n} = -\mathbf{S}_{NL}(\mathbf{H}_b, \mathbf{H}_b, 2) \cdot \mathbf{n} \text{ for } X_3 = \pm h,$$

$$\nabla \cdot (\mathbf{S}_L(\mathbf{H}_{ab})) - \rho \ddot{\mathbf{u}}_{ab} = -\nabla \cdot (\mathbf{S}_{NL}(\mathbf{H}_a, \mathbf{H}_b, 2)), \quad (35)$$

$$\mathbf{S}_L(\mathbf{H}_{ab}) \cdot \mathbf{n} = -\mathbf{S}_{NL}(\mathbf{H}_a, \mathbf{H}_b, 2) \cdot \mathbf{n} \text{ for } X_3 = \pm h.$$

The weak nonlinearity allows the forcing functions on the right hand side of the nonhomogeneous equations for the secondary wave fields, Eqs. (33)–(35), to be written in terms of the displacement gradients of the primary wave fields. The planar displacement fields associated with the primary wave fields a and b are taken to be

$$\mathbf{u}_a = \operatorname{Re}(\mathbf{U}_a(X_3)e^{i[\mathbf{K}_a \cdot \mathbf{p}(X_1, X_2) - \omega_a t]}), \quad (36)$$

$$\mathbf{u}_b = \operatorname{Re}(\mathbf{U}_b(X_3)e^{i[\mathbf{K}_b \cdot \mathbf{p}(X_1, X_2) - \omega_b t]}).$$

where \mathbf{p} is the position vector to the point of interest and \mathbf{K} is the wave vector, which can be written as $\mathbf{K} = k\mathbf{r}$, with k being the scalar wavenumber and \mathbf{r} being the unit direction vector.

D. Solution methodology for plates

The solution to the boundary value problems given by Eqs. (31) and (32) provides the primary wave fields and are obtained in the same manner as was Eq. (13) with the traction-free boundary conditions. More challenging to solve are the boundary value problems given by Eqs. (33) and (34) for self-interactions and Eq. (35) for mutual interactions. In order to demonstrate the procedure using the normal mode expansion, the solution to Eq. (33) will be described. The solutions to Eqs. (34) and (35) are similar, although the equations get more complicated for the non-collinear wave interactions that are possible with Eq. (35). The solution to the self-interaction problem, which generates second harmonics, is outlined next. The solution considers only second order interactions but can be applied to higher order interactions with due care of completeness and consistency; i.e., by further expanding Eq. (22) and assessing the associated higher order exponential functions.^{29,43}

For self-interactions, the primary displacement field in Eq. (36) can be written more simply as

$$\mathbf{u}_a = \operatorname{Re}(\mathbf{U}_a(X_3)e^{i[k_a X_1 - \omega_a t]}). \quad (37)$$

The nonlinear stress in Eq. (28) drives the solution and is comprised of terms having the following exponential functions for second order interactions: $e^{\pm i[(\mathbf{K}_a \pm \mathbf{K}_b) \cdot \mathbf{p}(X_1, X_2) - (\omega_a \pm \omega_b)t]}$. Self-interaction can be taken to be a special case of mutual interactions where $\omega_b = \omega_a = \omega$ and $\mathbf{K}_b = \mathbf{K}_a = \hat{\mathbf{i}}$, giving the second harmonic and the quasi-static pulse for this special case of monochromatic primary waves. $\hat{\mathbf{i}}$ is the basis vector in the X_1 -direction. The second harmonic wave field, therefore, involves nonlinear stress terms comprised of the exponential functions $e^{\pm i[2k_a X_1 - 2\omega_a t]}$.

The secondary wave field is determined by imposing the normal mode expansion,^{37,50} as in de Lima and Hamilton,²⁵ who actually solved the boundary value problem in Eq. (35) for second order interactions. Furthermore, the solution to the non-collinear wave mixing problem was given by Hasanian and Lissenden.⁵¹ But as noted above, only the solution to Eq. (33) is provided here. The normal mode expansion relies upon the orthogonality of the modes. To determine the orthogonality relation, Auld⁵⁰ derived the complex reciprocity relation, from which we get

$$\nabla \cdot [\mathbf{S}_1 \mathbf{V}_2^* + \mathbf{S}_2^* \mathbf{V}_1] = \frac{\partial}{\partial t} [\rho \mathbf{V}_2^* \cdot \mathbf{V}_1 + \mathbf{S}_2^* \cdot \mathbf{E}_1] - \mathbf{V}_2^* \cdot \mathbf{F}_1 - \mathbf{V}_1 \cdot \mathbf{F}_2^*, \quad (38)$$

where * indicates the complex conjugate and the subscripts 1 and 2 denote two different wave field solutions for the velocity, stress, strain, and source terms (\mathbf{V} , \mathbf{S} , \mathbf{E} , and \mathbf{F} , respectively). Auld⁵⁰ then formulated the modal orthogonality relation as

$$i[k_n^* - k_m] P_{mn} = 0$$

$$\text{where } P_{mn} = -\frac{1}{4} \int_{-h}^h \frac{1}{4} [\mathbf{S}_m(X_3) \mathbf{V}_n^*(X_3) + \mathbf{S}_n^*(X_3) \mathbf{V}_m(X_3)] \cdot \hat{\mathbf{i}} dX_3$$

$$\text{such that}$$

$$P_{mm} = 0 \text{ for } m \neq n$$

$$P_{mm} = \operatorname{Re} \left(-\frac{1}{8} \int_{-h}^h \mathbf{S}_m(X_3) \mathbf{V}_m^*(X_3) \cdot \hat{\mathbf{i}} dX_3 \right) \text{ for } m = n \quad (39)$$

for modes m and n . In Eq. (39), \mathbf{S} and \mathbf{V} are the modal stress and velocity, respectively, and we recognize P_{mm} to be the average power flow in the waveguide. As described below, the complex reciprocity relation will also be used to determine the modal coefficients $A_m(X_1)$, which are themselves defined subsequently.

Start by expanding the linear part of the secondary stress and velocity fields in terms of the possible modes m ,

$$\mathbf{S}_L(\mathbf{H}_{aa}) = \operatorname{Re} \left(\sum_{m=1}^{\infty} A_m(X_1) \mathbf{S}_m(X_3) e^{-i2\omega_a t} \right), \quad (40)$$

$$\mathbf{V}(\mathbf{H}_{aa}) = \dot{\mathbf{u}}(\mathbf{H}_{aa}) = \operatorname{Re} \left(\sum_{m=1}^{\infty} A_m(X_1) \mathbf{V}_m(X_3) e^{-i2\omega_a t} \right), \quad (41)$$

where the modal variables are computed from the displacement wavestructure \mathbf{U}_m ,

$$\begin{aligned}\mathbf{S}_m &= \frac{\lambda}{2} \operatorname{tr}(\mathbf{H}_m + \mathbf{H}_m^T) \mathbf{I} + \mu(\mathbf{H}_m + \mathbf{H}_m^T), \\ \mathbf{V}_m &= \dot{\mathbf{U}}_m, \quad \mathbf{H}_m = \nabla \mathbf{U}_m.\end{aligned}\quad (42)$$

The solution requires determination of the modal coefficients $A_m(X_1)$. To this end, we again apply the complex reciprocity relation, Eq. (38), letting wave field 1 be the modal expansion of the secondary field at 2ω ,

$$\mathbf{V}_1 = \operatorname{Re} \left(\sum_{m=1}^{\infty} A_m(X_1) \mathbf{V}_m(X_3) e^{-i2\omega t} \right), \quad (43)$$

$$\mathbf{S}_1 = \operatorname{Re} \left(\sum_{m=1}^{\infty} A_m(X_1) \mathbf{S}_m(X_3) e^{-i2\omega t} \right). \quad (44)$$

The nonlinear source, or driving force, terms come from the nonlinearity in the primary wave field given in Eq. (28),

$$\mathbf{F}_1 = \nabla \cdot \mathbf{S}_{NL} = \operatorname{Re}(\nabla \cdot \mathbf{S}_{NL}^{(1,1)}(X_3) e^{-i2[kX_1 - \omega t]}), \quad (45)$$

where $\mathbf{S}_{NL}^{(1,1)}$ is obtained by substituting the primary wave field into Eq. (27) with $b = a$, which interacts with itself, hence the notation (1,1). Furthermore, let wave field 2 be an arbitrary mode n of the secondary field at 2ω ,

$$\mathbf{V}_2 = \operatorname{Re}(\mathbf{V}_n(X_3) e^{-i[k_n X_1 - 2\omega t]}), \quad (46)$$

$$\mathbf{S}_2 = \operatorname{Re}(\mathbf{S}_n(X_3) e^{-i[k_n X_1 - 2\omega t]}), \quad (47)$$

$$\mathbf{F}_2 = 0. \quad (48)$$

With these wave fields, the complex reciprocity relation in Eq. (38) reduces to

$$\begin{aligned}\int_{-h}^h \frac{\partial}{\partial X_1} [\mathbf{S}_1 \mathbf{V}_2^* + \mathbf{S}_2^* \mathbf{V}_1] \cdot \mathbf{n}_1 dX_3 + [\mathbf{S}_1 \mathbf{V}_2^* + \mathbf{S}_2^* \mathbf{V}_1] \cdot \mathbf{n}_3|_{-h}^h \\ = - \int_{-h}^h \mathbf{V}_2^* \cdot \mathbf{F}_1 + \mathbf{V}_1 \cdot \mathbf{F}_2^* dX_3.\end{aligned}\quad (49)$$

Substituting the wave fields into Eq. (49) and some algebraic manipulation enables us to obtain the ordinary differential equation

$$\begin{aligned}\left[-ik_n^* + \frac{d}{dX_1} \right] A_m(X_1) &= \frac{f_n}{4P_{mn}} e^{i2kX_1}, \\ m &= 1, 2, 3, \dots,\end{aligned}\quad (50)$$

where P_{mn} is defined in Eq. (39) and

$$\begin{aligned}f_n &= f_n^{vol} + f_n^{surf}, \\ f_n^{vol} &= \frac{1}{2} \int_{-h}^h \mathbf{V}_n^* \cdot [\nabla \cdot \mathbf{S}_{NL}^{(1,1)}(X_3)] dX_3, \\ f_n^{surf} &= -\frac{1}{2} \mathbf{V}_n^* \cdot \mathbf{S}_{NL}^{(1,1)}(X_3) \cdot \mathbf{n}_3|_{-h}^h.\end{aligned}\quad (51)$$

f_n^{vol} and f_n^{surf} can be considered to be nonlinear body force and nonlinear surface traction, which are source-like terms.

Equation (50) can be solved using an integration factor

$$A_m(X_1) = \begin{cases} \frac{f_n}{4P_{mn}} X_1 e^{i2kX_1} & \text{for } 2k - k_n^* = 0, \\ \frac{i}{k_n^* - 2k} \frac{f_n}{4P_{mn}} [e^{i2kX_1} - e^{ik_n^* X_1}] & \text{for } 2k - k_n^* \neq 0. \end{cases} \quad (52)$$

The first solution occurs when the wavenumber of the secondary mode matches $2k$; in this case, the phase velocity of the secondary wave mode n , $c_p = 2\omega/2k$, matches that of the primary mode and its wavelength $\lambda = c_p/2f$ is half the wavelength of the primary wave mode. Thus, the secondary waves are said to be *phase-matched* or *synchronized* with the primary waves. In addition, there must be *nonzero power flow*, $f_n \neq 0$, to the secondary mode n . When these two conditions are met, the secondary waves and primary waves are said to have *internal resonance*. The second harmonic waves are *cumulative* in this case, as they increase linearly in amplitude with propagation distance (although this is limited to continuous plane waves in a lossless medium, while the secondary wave amplitude is much less than the primary wave amplitude). Due to the orthogonality relation, the secondary wave field is composed of mode $m = n$. The second solution in Eq. (52) is a bounded oscillation having a spatial periodicity or beat length.²⁵ The non-phase matched condition has been investigated by Matsuda and Biwa⁵² and others.^{53,54}

V. INTERNALLY RESONANT WAVES IN PLATES

We now aim to leverage what is known about the general characteristics of nonlinear guided waves in plates in order to develop methods to use them for ultrasonic NDE. First, the cumulative nature of the secondary wave field is investigated with respect to the requirements for nonzero power flow and synchronism. Then, the importance of group velocity matching is discussed, followed by the definition of the mixing power, which is intended to provide a measure of the strength of the nonlinearity.

The internal resonance conditions for waves in plates that result from Eq. (52) provide valuable information about which cumulative secondary wave modes can be generated by specific primary wave modes. Analogous internal resonance conditions for hollow cylinders have been investigated as well,^{41,55,56} but are not included in this section.

A. Nonzero power flow

Consider first the nonzero power flow criteria that f_n in Eq. (51) cannot be zero to have internal resonance. f_n provides the

nonlinear driving force, thus if there is no driving force then there is no nonlinearity. A parity analysis can be conducted to determine to which secondary wave modes there is no power flow based on the symmetry or antisymmetry of the wavestructure.^{25,28,29,57,58} The parity analysis involves using the symmetric/antisymmetric nature of the wavestructure to ascertain whether f_n^{vol} and f_n^{surf} in Eq. (51) are zero. Let us define generic symmetric and antisymmetric functions with respect to the X_3 axis as $S = S(X_3)$ and $A = A(X_3)$, respectively. The symmetry/antisymmetry of the wave field variables $\mathbf{u}, \mathbf{v}, \mathbf{H}, \mathbf{S}_{NL}^{(1,1)}, \nabla \cdot \mathbf{S}_{NL}^{(1,1)}$ is given in Table I for Lamb wave modes and SH wave modes, where the $\mathbf{S}_{NL}^{(1,1)}$ and $\nabla \cdot \mathbf{S}_{NL}^{(1,1)}$ variables are evaluated from Eq. (28). As a reminder, $\mathbf{u}, \mathbf{v}, \mathbf{H}$, in Eq. (51) for f_n^{vol} and f_n^{surf} represent the secondary wave field, while the $\mathbf{S}_{NL}^{(1,1)}$ and $\nabla \cdot \mathbf{S}_{NL}^{(1,1)}$ are the driving forces from the primary wave field. Observe from Table I that the symmetry of $\mathbf{S}_{NL}^{(1,1)}$ and $\nabla \cdot \mathbf{S}_{NL}^{(1,1)}$ is independent of the wave mode.

Consider, for example, a symmetric SH primary wave field generating secondary Lamb waves. From Eq. (51) the nonlinear body force for a symmetric secondary Lamb wave field is

$$f_n^{vol} = \frac{1}{2} \int_{-h}^h \begin{Bmatrix} S \\ 0 \\ A \end{Bmatrix} \cdot \begin{Bmatrix} S \\ 0 \\ A \end{Bmatrix} dX_3 \neq 0, \quad (53)$$

while for an antisymmetric secondary Lamb wave field it is

$$f_n^{vol} = \frac{1}{2} \int_{-h}^h \begin{Bmatrix} A \\ 0 \\ S \end{Bmatrix} \cdot \begin{Bmatrix} S \\ 0 \\ A \end{Bmatrix} dX_3 = 0. \quad (54)$$

Also from Eq. (51), the nonlinear surface traction for a symmetric secondary Lamb wave field is

$$f_n^{surf} = -\frac{1}{2} \begin{Bmatrix} S \\ 0 \\ A \end{Bmatrix} \cdot \begin{Bmatrix} S & 0 & A \\ 0 & S & 0 \\ A & 0 & S \end{Bmatrix} \begin{Bmatrix} 0 \\ 0 \\ 1 \end{Bmatrix} \Big|_{-h}^h \neq 0, \quad (55)$$

TABLE I. Symmetric (S) and antisymmetric (A) terms in the wave field variables.

Mode type	\mathbf{u} and \mathbf{v}	\mathbf{H}	$\mathbf{S}_{NL}^{(1,1)}$	$\nabla \cdot \mathbf{S}_{NL}^{(1,1)}$
Symmetric Lamb	$\begin{Bmatrix} S \\ 0 \\ A \end{Bmatrix}$	$\begin{bmatrix} S & 0 & A \\ 0 & 0 & 0 \\ A & 0 & S \end{bmatrix}$	$\begin{bmatrix} S & 0 & A \\ 0 & S & 0 \\ A & 0 & S \end{bmatrix}$	$\begin{Bmatrix} S \\ 0 \\ A \end{Bmatrix}$
Antisymmetric Lamb	$\begin{Bmatrix} A \\ 0 \\ S \end{Bmatrix}$	$\begin{bmatrix} A & 0 & S \\ 0 & 0 & 0 \\ S & 0 & A \end{bmatrix}$	$\begin{bmatrix} 0 & S & 0 \\ A & 0 & S \end{bmatrix}$	$\begin{Bmatrix} 0 \\ A \\ 1 \end{Bmatrix}$
Symmetric SH	$\begin{Bmatrix} 0 \\ S \\ 0 \end{Bmatrix}$	$\begin{bmatrix} 0 & 0 & 0 \\ S & 0 & A \\ 0 & 0 & 0 \end{bmatrix}$	$\begin{bmatrix} S & 0 & A \\ 0 & S & 0 \\ A & 0 & S \end{bmatrix}$	$\begin{Bmatrix} S \\ 0 \\ A \end{Bmatrix}$
Antisymmetric SH	$\begin{Bmatrix} 0 \\ A \\ 0 \end{Bmatrix}$	$\begin{bmatrix} 0 & 0 & 0 \\ A & 0 & S \\ 0 & 0 & 0 \end{bmatrix}$	$\begin{bmatrix} 0 & S & 0 \\ A & 0 & S \end{bmatrix}$	$\begin{Bmatrix} 0 \\ A \\ 1 \end{Bmatrix}$

while for an antisymmetric secondary Lamb wave field it is

$$f_n^{surf} = -\frac{1}{2} \begin{Bmatrix} A \\ 0 \\ S \end{Bmatrix} \cdot \begin{bmatrix} S & 0 & A \\ 0 & S & 0 \\ A & 0 & S \end{bmatrix} \begin{Bmatrix} 0 \\ 0 \\ 1 \end{Bmatrix} \Big|_{-h}^h = 0. \quad (56)$$

Thus, a symmetric SH primary wave field can generate a secondary symmetric Lamb wave field but not an antisymmetric one. This result applies whether the wave fields are synchronized or not. Table II, which is for the mutual interaction of two collimated waves from Liu,⁵⁹ indicates to which types of secondary wave fields power flows from the mutual interaction of two primary waves. Four types of wave fields are considered:

SRL = symmetric Rayleigh-Lamb (same as “symmetric Lamb”) wave field

ARL = antisymmetric Rayleigh-Lamb (same as “antisymmetric Lamb”) wave field

SSH = symmetric shear-horizontal wave field

ASH = antisymmetric shear-horizontal wave field.

While the parity analysis provides valuable information about which wave modes do not lead to internal resonance, it is worth pointing out that it does not provide information about how much power is transferred. In closure, the results of the parity analysis on third order wave interactions are given by Liu *et al.*,⁴³ while results for non-collinear wave fields are given by Hasanian and Lissenden.⁵¹ Likewise, power flow in hollow cylinders has been analyzed by Liu *et al.*^{41,55}

B. Synchronization

We now seek to determine when the primary and secondary wave fields are synchronized as per the conditional statement that $2k - k_n^* = 0$ in Eq. (52); i.e., the frequency-wavenumber pairs (ω, k) and $(2\omega, 2k)$ lie on dispersion curves of propagating wave modes. The dispersion relations for Lamb waves and SH waves are Eqs. (15) and (16), respectively. While a graphical approach to

TABLE II. Does power flow from the mutual interaction of two collimated primary wave fields to a second order wave field? After Liu.⁵⁹

Interacting primary wave fields	Type of secondary wave field			
	SRL	ARL	SSH	ASH
SRL-SRL				
ARL-ARL				
SSH-SSH	Yes	No	No	No
ASH-ASH				
SRL-ARL				
SSH-ASH	No	Yes	No	No
SRL-SSH				
ARL-ASH	No	No	Yes	No
SRL-ASH				
ARL-SSH	No	No	No	Yes

finding synchronism points is common, a rigorous mathematical approach is also available⁶⁰ and can provide more information than would be gleaned from looking at the dispersion curves themselves. For simplicity, we again consider second harmonic generation from self-interaction, but the approach is applicable to mutual interactions and higher (e.g., third) harmonics. First, consider the case of both primary and secondary wave fields being symmetric Lamb waves. The right-hand side of Eq. (15) is the same for both (ω, k) and $(2\omega, 2k)$, therefore

$$\frac{\tan(qh)}{\tan(ph)} = \frac{\tan(2qh)}{\tan(2ph)}, \quad (57)$$

where p and q were defined after Eq. (15). A few manipulations lead to

$$2 \sin(ph) \sin(qh) [\cos(2ph) - \cos(2qh)] = 0, \quad (58)$$

whose solutions are

$$\begin{aligned} qh &= n\pi, \\ ph &= n\pi, \\ qh \pm ph &= n\pi, \end{aligned} \quad (59)$$

where n is an arbitrary whole number. There are many ways in which Eq. (58) can be satisfied. Consider the first solution in Eq. (59) first, where $p \neq q$. Thus, Eq. (15) becomes

$$\frac{\tan(n\pi)}{\tan(ph)} = - \left[\frac{4k^2 pq}{[(q^2 - k^2)^2]} \right] = 0, \quad (60)$$

which is satisfied when $k = 0$, which occurs as $c_p \rightarrow \infty$ at the mode cutoffs. However, this second harmonic will not propagate because standing waves occur at the mode cutoffs. Another possibility is that $p = 0$, which leads to

$$\omega = \frac{n\pi}{h} \frac{c_L c_T}{\sqrt{c_L^2 - c_T^2}}, \quad k = \frac{\omega}{c_L}, \quad c_p = c_L, \quad (61)$$

which occurs for all symmetric Lamb modes ($n = 1, 2, \dots$).

The second solution in Eq. (59) leads to

$$\omega = \frac{n\pi}{h} \frac{\sqrt{2} c_L c_T}{\sqrt{2c_T^2 - c_L^2}}, \quad k = \frac{\omega}{\sqrt{2} c_T}, \quad c_p = \sqrt{2} c_T, \quad (62)$$

which is limited by the requirement that $\sqrt{2} c_T \geq c_L$. These are the Lamé modes.

The third solution in Eq. (59) results in conditions for both symmetric and antisymmetric Lamb waves being satisfied, $\tan(qh) = \tan(ph)$, which occurs at wave mode crossing points.

Likewise, a similar analysis can be conducted to show that antisymmetric primary Lamb waves can generate symmetric second harmonic Lamb waves when

$$\omega = \frac{[2n+1]\pi}{2h} \frac{\sqrt{2} c_L c_T}{\sqrt{2c_T^2 - c_L^2}}, \quad k = \frac{\omega}{\sqrt{2} c_T}, \quad c_p = \sqrt{2} c_T, \quad (63)$$

which is also limited by the requirement that $\sqrt{2} c_T \geq c_L$.

Power flow analysis showed that primary Lamb waves could not generate second harmonic SH waves, but the reverse can occur, and the synchronism can be analyzed as above. The results indicate that primary SH waves can generate synchronized second harmonic symmetric Lamb waves when the second harmonic 2ω is

- A mode cutoff;
- A mode crossing point;
- $2\omega = \frac{n\pi}{h} \frac{c_L c_T}{\sqrt{c_L^2 - c_T^2}}$, $c_p = c_L$.

The third condition, when $c_p = c_L$, was investigated by Liu *et al.*⁵⁸ A finite element simulation of the second condition, where the SH0 and S0 Lamb wave modes cross, is described in Sec. VIII B.

C. Group velocity matching

Internal resonance, as given by Eq. (52), is not reliant upon the group velocity of the secondary waves being equal to the group velocity of the primary waves. The formulation of Eq. (52) presumes that the planar waves are continuous, and therefore they interact continuously, enabling power to flow to the secondary mode as they propagate together. However, it is common to use a toneburst excitation in NDE applications, creating a wave packet of a finite length. Thus, if the group velocities of the primary waves and secondary waves are sufficiently different to cause the wave packets to separate, then the interactions cease and the cumulative nature of the secondary waves changes as shown in Hasanian and Lissenden.⁵¹ The subject of group velocity matching has been a rather controversial subject, probably because it is not a strict requirement, but rather provides longer wave interaction periods, which enables more energy transfer to the secondary waves, further discussion can be found in Refs. 22, 27, 28, 61–63, and 64. Likewise, the mutual interaction of counter-propagating and non-collinear waves is dependent upon the duration of the wave mixing as discussed by Hasanian and Lissenden.⁵¹

D. Mixing power

Given the large number of propagating guided wave modes and the limitations associated with satisfying internal resonance, the question of which primary waves will generate second harmonic waves that are actually useful for NDE naturally arises. This is a complex issue with many layers. Here we address the issue of power flow from the primary waves to the secondary waves. Section VI will address the next layer and provide information about which Lamb and SH wave modes at prescribed frequencies generate internally resonant second harmonics. Other layers, such as transducer selection and signal processing are introduced in Sec. VII.

We seek to quantify the power flow from primary waves to secondary waves, whether by self-interaction or mutual interaction. Toward this end, we start with the general wave mixing problem between planar primary waves A and B that interact at an angle θ and generate secondary waves that propagate at angle γ . In this broader problem, Eq. (52) becomes⁵¹

$$A_m(X_1, X_2) = \begin{cases} \frac{f_n}{4\tilde{P}_{mn}} \frac{[\mathbf{K}_a \pm \mathbf{K}_b] \cdot \mathbf{p}(X_1, X_2)}{|\mathbf{K}_a \pm \mathbf{K}_b|} e^{i[\mathbf{K}_a \pm \mathbf{K}_b] \cdot \mathbf{p}(X_1, X_2)} & \text{for } \mathbf{K}_n^* = \mathbf{K}_a \pm \mathbf{K}_b, \\ \frac{-i}{|\mathbf{K}_n^* - [\mathbf{K}_a \pm \mathbf{K}_b]|} \frac{f_n}{4\tilde{P}_{mn}} [e^{i\mathbf{K}_n^* \cdot \mathbf{p}(X_1, X_2)} - e^{i[\mathbf{K}_a \pm \mathbf{K}_b] \cdot \mathbf{p}(X_1, X_2)}] & \text{for } \mathbf{K}_n^* \neq \mathbf{K}_a \pm \mathbf{K}_b, \end{cases} \quad (64)$$

$$\begin{aligned} \tilde{P}_{mn} &= \mathbf{P}_{mn} \cdot \mathbf{r}_m, \\ \mathbf{P}_{mn} &= -\frac{1}{4} \int_{-h/2}^{h/2} \frac{1}{4} [\mathbf{S}_m(X_3) \mathbf{V}_n^*(X_3) + \mathbf{S}_n^*(X_3) \mathbf{V}_m(X_3)] dX_3, \end{aligned} \quad (65)$$

where \mathbf{P}_{mn} is the Poynting vector integrated through the thickness of the plate, while \tilde{P}_{mn} projects that vector in the direction of the secondary waves. Recall that \mathbf{p} and \mathbf{r} were defined after Eq. (36). Let us now write the secondary wave field using the subscript r for the internally resonant mode that dominates the expansion of possible modes,

$$\mathbf{u}_r = \operatorname{Re}(A_r(X_1, X_2) \mathbf{U}_r(X_3) e^{-i[\omega_a \pm \omega_b]t}), \quad (66)$$

where A_r is the modal coefficient and \mathbf{U}_r is the wavestructure. But, it can be also written as

$$\mathbf{u}_r = \operatorname{Re}(M_{ab,r} \mathbf{U}_r(X_3) [\mathbf{r}_r \cdot \mathbf{p}(X_1, X_2)] e^{i[\mathbf{K}_r \cdot \mathbf{p}(X_1, X_2) - \omega_r t]}), \quad (67)$$

where now we have

$$M_{ab,r} = \frac{f_n}{4P_{rr}}, \quad (68)$$

$$\mathbf{r}_r = \frac{\mathbf{K}_a \pm \mathbf{K}_b}{|\mathbf{K}_a \pm \mathbf{K}_b|}. \quad (69)$$

For this form of the solution [Eq. (67)], it is important to normalize the wavestructure vector $\mathbf{U}_r(X_3)$ such that the maximum value of any component is unity. We can call $M_{ab,r}$ the mixing power associated with wave interaction, whether due to self-interaction (where $a=b$) or mutual interaction. Equation (68) quantifies the power flow from primary waves to secondary waves and provides a convenient way to compare different types of wave interactions. It does not however consider the size of the wave mixing zone because the waves are considered to be planar continuous waves. Values of the mixing power will be given in Sec. VI.

VI. PRIMARY WAVE SELECTION GUIDELINES

Sections IV and V provide a specialized analysis for plates. This section uses that information to provide some guidelines for selecting which primary wave modes and at what frequency to actuate them in order to generate second harmonics from the material nonlinearity. Although the majority of the section applies to plates, pipes and arbitrary cross sections are also briefly discussed.

A. Plates

The simple geometry of a plate enabled the internal resonance conditions to be determined based on Eq. (52). These two

conditions, nonzero power flow and synchronism, were analyzed in considerable detail in Sec. V A such that it is now possible to identify which wave modes propagating at a prescribed frequency will generate cumulative second harmonic waves. While these will be presented as distinct internal resonance points, in reality each internal resonance point is enclosed within a region of finite-size due to the frequency bandwidth associated with the toneburst excitation and phase velocity bandwidth associated with the finite transducer size (referred to as the source influence by Rose³⁷) and investigated by Matsuda and Biwa.⁵²

Eight points where primary waves can generate internally resonant second harmonics through self-interaction are marked in Fig. 13, where the phase velocity dispersion curves for Lamb waves and SH waves are plotted. The specifics for each of the internal resonance points for self-interaction are compiled in Table III. The mode pair designates the primary wave modes and second harmonic wave modes, respectively. The fd product is given for the primary wave mode, and of course the fd of the second harmonic is simply twice that value. The phase velocity of primary and second harmonic waves are synchronized, but the group velocities may not be synchronized. Finally, the far-right column gives the mixing power for the self-interaction from Eq. (68). This important information was also provided in the book chapter by Lissenden and Hasanian.¹⁵

The internal resonance points occur at the longitudinal wave speed (points 1, 2, 5–7), the transverse wave speed (point 4), mode intersection points (points 3 and 8), and at mode cutoffs (no points shown). Note that points 1 and 6 occur at the same frequency, as do points 3 and 8. The mixing power for self-interaction

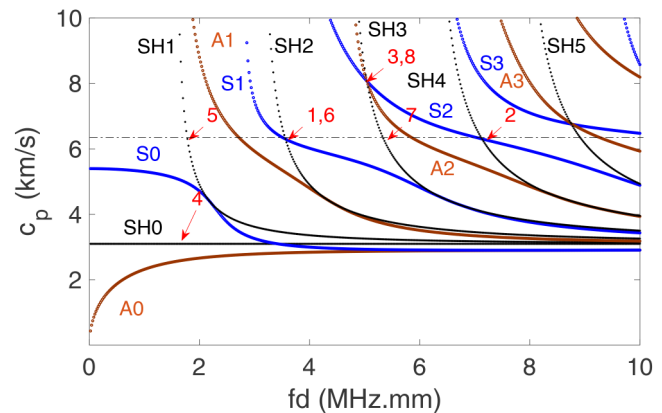


FIG. 13. Phase velocity dispersion curves for an aluminum plate with internal resonance points marked. $c_L = 6.35$ km/s and $c_T = 3.10$ km/s.

TABLE III. Internal resonance points marked in Fig. 13—Aluminum plate.

Point	Mode pair	fd (MHz mm)	c_p (km/s)	c_g (km/s)	M_{aa_r} (mm $^{-2}$)
1	S1–S2	3.56	c_L	4.3–4.3	15.4
2	S2–S4	7.12	c_L	4.3–4.3	59.8
3	S2/A2–S4	~5.0	~8.1	~3.7–1.7	10.2
4	SH0–S0	1.68	c_T	3.1–2.4	4.48
5	SH1–S1	1.78	c_L	1.5–4.3	6.32
6	SH2–S2	3.56	c_L	1.5–4.3	22.2
7	SH3–S3	5.34	c_L	1.5–4.3	56.3
8	SH3–S4	~5.0	~8.1	1.3–1.4	51.4

of a longitudinal bulk wave provides a reference for the mixing powers given in Table III. For primary longitudinal bulk wave frequencies of 1.00 and 3.56 MHz the mixing powers are 1.89 and 24.6 mm $^{-2}$, respectively. The simplest explanation for why the mixing power increase with frequency is so large can be traced back to Eq. (6), which shows that the amplitude of the second harmonic increases with the square of the wavenumber. Since the wavenumber is proportional to the frequency, for a bulk wave the mixing power should increase with the square of the frequency. The frequency effect on guided waves is more complicated due to the different wavestuctures that exist. For internal resonance point 1 the primary waves are the S1 Lamb mode, and they generate the second harmonic S2 Lamb mode. The phase velocities are matched and equal to the longitudinal wave speed, and the group velocities are also matched. These modes at these frequencies are known as “nonleaky modes” because the u_3 displacement component at the plate surface is zero and therefore energy does not leak into a surrounding fluid. This nonleaky characteristic also makes them more challenging to send and receive.

As noted above, the S1 and SH2 modes at $fd = 3.56$ MHz-mm both generate the S2 mode as a second harmonic (these are internal resonance points 1 and 6). Surprisingly, the SH2 primary waves actually have a higher mixing power than do the S1 primary waves (22.15 to 15.4 mm $^{-2}$), which implies that given the same input energy that the SH2 waves would transfer more energy to the S2 second harmonic waves than do S1 waves. The mixing power in Eq. (68) comes from f_n in Eq. (51) and P_{rr} in Eq. (39). Since P_{rr} depends only on the second harmonic, which is the S2 mode at $2fd$ in both cases, the difference must come from the nonlinear driving force f_n in Eq. (51), which in turn comes from the nonlinear stress derived from the primary wave field in Eq. (27) and its divergence.

Even though there are an infinite number of points on the dispersion curves of propagating modes, the internal resonance conditions place severe limitations on the primary mode selection options for plates. That the primary and secondary waves must interact for the second harmonic to be cumulative places further limitations on selection options based on the group velocities being similar. In addition, the excitability of the primary waves and receivability of the secondary waves are also important considerations as transducer availability and capability play an important role in developing a measurement technique.

Given the limitations of internally resonant second harmonics, we seek to expand the design space for NDE applications. One approach is to relax the synchronism requirement. Although not exactly phase-matched, the S0 mode provides an alternative either in the low frequency regime (as analyzed by Chillara and Lissenden⁵³ and Zuo *et al.*⁵⁴) or the high frequency regime where both primary and secondary waves are quasi-Rayleigh waves. Another alternative is to use third harmonics. Internal resonance points for third harmonics generated by Lamb and SH waves modes are given by Liu *et al.*⁴³ SH waves do not generate SH second harmonics, but they do generate SH third harmonics. The use of the SH0 wave mode has the advantage that it is nondispersive and has a uniform wavestructure.^{65,66} In fact, any SH mode at any frequency will generate a phase-matched third harmonic through self-interaction—they are holo-internal-resonant.⁴³ Yet another approach to broaden the design space for nonlinear guided wave NDE is to use wave mixing to induce mutual interactions as described by Hasanian and Lissenden.^{51,67} Tables containing internal resonance points for second order harmonics obtained from co-directional, counter-propagating, non-collinear wave mixing are given by Lissenden and Hasanian in Ref. 15.

B. Hollow cylinders

There are many similarities between axisymmetric waves in hollow cylinders and planar waves in plates. Except in the low frequency regime, the dispersion curves are similar, thus the internal resonance points are effectively the same.⁵⁵ Flexural wave propagation is not axisymmetric and requires a different mathematical modeling approach.⁴¹ The interested reader is referred to Liu *et al.* for applications of nonlinear flexural waves.⁵⁶

C. Arbitrary cross section

The propagating modes in waveguides having an arbitrary cross section can be analyzed using SAFE as summarized in Sec. III C. The dispersion curves for a rail section are shown in Fig. 11. Methodology to analyze nonlinear waves in arbitrary cross sections using SAFE results is provided by Nucera and Lanza di Scalea.^{31,68} Synchronism can be analyzed simply from the wavenumbers (phase velocities). But internal resonance requires both synchronism and nonzero power flow. By knowing the nonlinear driving forces, the power flow from the primary to secondary mode can also be assessed and appropriate modes selected.

VII. MEASUREMENT METHODS

Chapter 3 by Lissenden and Hasanian in Ref. 15 describes the measurement of nonlinear guided waves in detail, thus to not be redundant, this section simply emphasizes the important considerations relative to actuation, reception, and signal processing. The key consideration in developing a nonlinear guided wave measurement setup to interrogate material state evolution is that the nonlinearity is weak, making the signal of interest very small. The guidelines in Sec. VI for selecting primary wave modes are intended to accentuate the nonlinearity and enhance the secondary waves. Beyond the selection of the primary and secondary wave modes and frequencies, primary waves having finite amplitude are highly

desirable because they are the source of the secondary waves. It is common for the amplitude of secondary waves to be two or three orders of magnitude less than that of the primary waves, leading to a challenging measurement. In this context finite amplitude means *as large as possible* within the elastic wave regime; i.e., no plastic strains because it is intended to be nondestructive evaluation. In reality, both the wave amplitude and the noise in the measurement system are of critical importance.

In most cases, ultrasonic testing relies on an electrical power source to generate a signal that is amplified and then sent to a transducer, which converts the electrical energy to elastic energy. Typically, piezoelectric and magnetostrictive materials enable that energy conversion through elastic-electric and elastic-magnetic coupling respectively (e.g., as described in Giurgiutiu's⁶⁹ Chap. 2). In piezoelectric materials, which are common for commercial transducers, the electrical input signal is limited by the breakdown voltage. The transducer output is dictated by both the input signal and the efficiency of the energy conversion, which for piezoelectric materials is characterized by the coupling coefficients⁶⁹ d_{33} , d_{31} , etc. The actuation of guided waves presents another layer of complexity in that typically the transducer is placed on the lateral boundary of the waveguide. Consequently, while guided wave modes have unique wavestuctures, the transducer placement is limited to the surface, and thus the *excitability* of a particular mode with a prescribed transducer depends in large part on the wavestucture, as discussed by Rose.³⁷ Moreover, the presence of multiple modes at the excitation frequency and the source influence make it difficult to preferentially actuate a prescribed mode.

Given the limitations identified above regarding the actuation of finite amplitude primary waves, the noise in the measurement system must be carefully managed. Nonlinear ultrasonic measurements are based on received signals at frequencies other than the excitation frequency, thus the noise in the frequency spectrum must be considered. Toneburst inputs are common for ultrasonic guided wave testing. For nonlinear ultrasonic guided wave testing the number of cycles in the burst should be maximized in order to minimize the frequency bandwidth so that the secondary waves are not obscured in the frequency spectrum. Both the generated burst signal and the period between bursts need to be as clean as possible. The received signal should be digitized at a high rate to limit the quantization error as described by Jhang *et al.* (Chap. 2, Ref. 15)

Time-synchronous signal averaging is used to reduce the incoherent noise within a specific measurement setup. The trade-off between incoherent noise reduction and testing time should be considered when selecting the number of averages; anywhere from 32 to 1024 averages have been used in the literature. But beyond simply averaging for one setup, the measurement repeatability must be proven because transducer coupling and positioning variation can lead to results that are not reproducible. If the transducer is affixed to the waveguide one time for multiple measurements, such as for structural health monitoring, there will certainly be less variability between measurements. However, if adhesive is used to affix the transducer, then degradation of the adhesive may need to be considered. For nondestructive testing or inspection, where the coupling and positioning of the transducer is established for each setup, repeatability is documented by repeated disassembly, re-assembly, re-test, and assessing the statistics of variation.

Nonlinearities exist in components of ultrasound measurement systems such as amplifiers, transducer materials, and the couplant. A low-pass filter placed between the amplifier and the transducer can minimize the frequency content above the excitation frequency. Likewise, the received signal can be split and bandpass filtered around the primary frequency and the secondary frequency. A narrowband transducer selected to receive the secondary frequency is likely to partially filter the excitation frequency. All of these issues must be considered when designing the measurement methods.

The remainder of this section discusses aspects specific to actuation, reception, and signal processing.

A. Actuation

The most common transducers for actuating ultrasonic guided waves can be categorized as:

- angle-beam—activation line on phase velocity dispersion curves is horizontal with the phase velocity determined by Snell's law³⁷;
- comb—the slope of the activation line on phase velocity dispersion curves is equal to the pitch of the elements in the comb³⁷ since the pitch determines the wavelength and $c_p = \lambda f$;⁶⁹
- wafer—a thin wafer bonded to the surface can be tuned to a mode based on its size and wavelengths of the possible modes at the excitation frequency.

Transducer selection includes not only which type of transducer to use for actuation, but also transducer material and couplant. Lithium niobate is often used as the active transducer material despite its coupling coefficients d_{33} , d_{31} , etc., being considerably lower than lead zirconate titanate (PZT). The purpose of couplant is to remove air from the wave path and thereby reduce the acoustic impedance mismatch. However, liquid couplant can introduce variability based on the layer thickness and heterogeneity, as well as nonlinearity. Thus, it is good practice to apply a known pressure to the transducer to give a repeatable couplant thickness. Without providing further discussion, we note that phased arrays can be used to focus wave energy at a predefined point of interest.^{70,71}

B. Reception

There are many ways to receive ultrasonic guided waves. Many receivers are significantly more sensitive to particle motion normal to the surface than tangent to it, especially if there is liquid couplant involved. If signal-to-noise ratio (SNR) is the most important consideration—since the amplitudes of the secondary waves are much smaller than the primary waves—then repeatability of the measurements is a close second. Successful measurements have been made with a piezoelectric contact transducer mounted on a wedge,⁷² angled air-coupled transducer,⁷³ laser interferometer,²⁷ shear transducer,⁵⁸ and polyvinylidene difluorine (PVDF) film.⁷⁴ The references cited are just examples and far from a complete list. The advantages of noncontact receivers are that they eliminate the potential variability associated with couplant and they simplify scanning along the wavevector direction to characterize the cumulative nature of the secondary waves. Confirming that the secondary waves are cumulative ensures that the source of the nonlinearity is

primarily due to the material and not just the instrumentation. Our experience with noncontact reception is that an angled air-coupled transducer provides better repeatability than a laser interferometer. This could be because the air-coupled transducer has a significantly larger area that provides intrinsic signal averaging, whereas the laser interferometer samples a very small spot, making it more susceptible to pointwise material variability.

C. Signal processing

Nonlinear ultrasonic measurements require information to be extracted at frequencies other than the excitation frequency, thus the fast Fourier transform (FFT) is an important tool, for which readers are referred elsewhere (e.g., Jhang *et al.*'s Chap. 2 in Ref. 15). In many cases, the objective of nonlinear ultrasonic testing is to determine a relative nonlinearity parameter, often denoted β' , which has its origin in Eq. (6), where the amplitude of the second harmonic is

$$A_2 = \frac{1}{8} \beta k^2 A_1^2 x \quad (70)$$

and therefore, in terms of wave amplitudes,

$$\beta = \frac{8A_2}{k^2 A_1^2 x}. \quad (71)$$

At a prescribed propagation distance,

$$\beta \propto \beta' = \frac{A_2}{A_1^2}. \quad (72)$$

It is common to take the spectral amplitudes at the primary and secondary frequencies obtained from voltage measurements to be proportional to the wave amplitudes at these frequencies. Similarly, the relative nonlinearity parameter for third harmonics is A_3/A_1^3 , and for wave mixing relative nonlinearity parameters such as $A_{f_a+f_b}/[A_{f_a}A_{f_b}]$ are common. The measurement of the relative nonlinearity parameter should be independent of the input voltage as is the case for region 1 in the third harmonic measurement by Lissenden *et al.*⁷⁵ shown in Fig. 14. The relative nonlinearity parameter increases with decreasing input voltage in region 2 because the true A_3 is below the noise floor and therefore not measurable.

Relative to bulk waves, guided waves provide a straightforward means to assess the cumulative behavior of the secondary waves. For example, nonlinear quasi-Rayleigh waves propagating in aluminum are seen to be cumulative in Fig. 15. The linear increase in the amplitude of second harmonics predicted by Eq. (52), for example, is for plane waves in lossless media, thus the effects of diffraction and attenuation may need to be taken into account when comparing experimental results with these predictions.

For waveguides where multiple wave modes are propagating at different group velocities, the amplitudes of the modes may need to be determined from a spectrogram (as shown in Fig. 16). In addition, FFTs can sometimes be avoided by using a phase inversion technique.^{76,77} Finally, we close this section by recognizing that

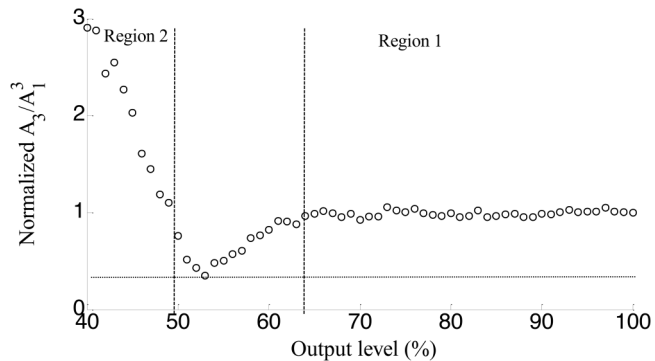


FIG. 14. A_3/A_1^3 for increasing voltage (output level) sent to a magnetostrictive transducer, which actuates SH0 waves in an aluminum plate. Reproduced with permission from IMECE2014-39699 (2014). Copyright 2014 ASME.

results of wave mixing experiments can be analyzed by computing a difference signal. Suppose we wanted to assess secondary waves generated by the mutual interaction of waves A and waves B. We would collect three sets of data: waves A alone, waves B alone, and waves A plus waves B. The nonlinearity associated with the mutual interaction would be apparent in the difference signal obtained from: $(A + B) - (A) - (B)$.^{67,70,74}

VIII. CASE STUDIES

The underlying principles of nonlinear ultrasonic guided waves applied to nondestructive evaluation are demonstrated through case studies in this section. Symmetric Lamb waves in plates generate internally resonant second harmonics in some special cases. In other cases, the primary and secondary waves are not exactly synchronized, but the results can still be useful.

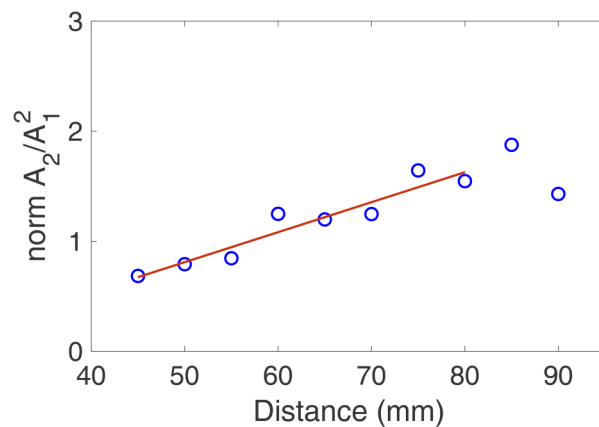


FIG. 15. Normalized nonlinearity parameter, A_2/A_1^2 , as a function of propagation distance for a quasi-Rayleigh wave in a thick aluminum plate. 25-cycle toneburst with 2 MHz central frequency sent from 2.25 MHz angle-beam transducer received from 5 MHz angle-beam transducer. Courtesy of Chaitanya Bakre.

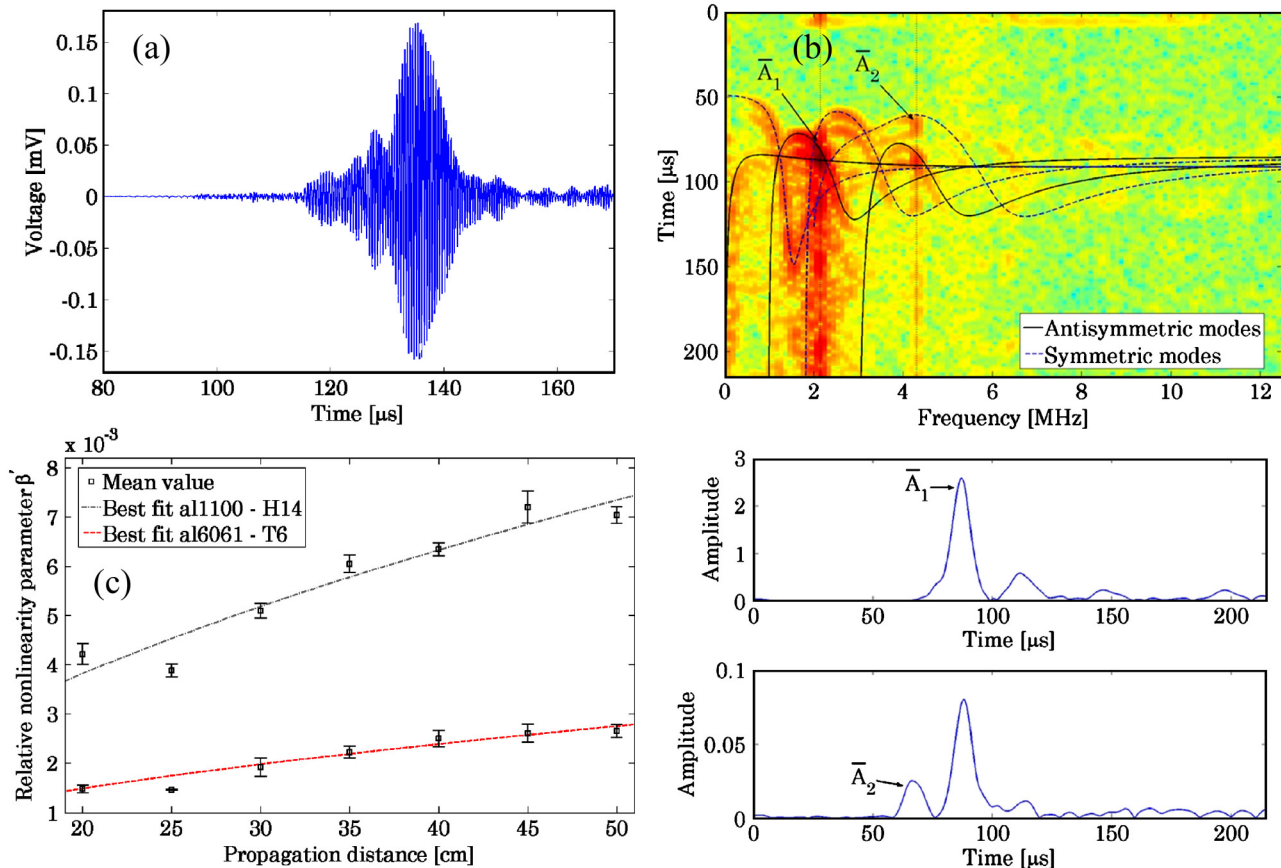


FIG. 16. 20-cycle toneburst excitation having 2.15 MHz center frequency on an aluminum plate: (a) received A-scan, (b) spectrogram and slices at 2.15 and 4.30 MHz, (c) cumulative relative nonlinearity parameter for two aluminum alloys. Reproduced with permission from Bermes *et al.*, *Appl. Phys. Lett.* **90**, 021901 (2007). Copyright 2007 AIP Publishing LLC.

Likewise, SH waves can generate second harmonics that are symmetric Lamb waves and third harmonics that are SH waves. A transient dynamics finite element simulation of nonlinear guided wave propagation in a plate is described in Sec. VIII B, which is entirely independent of the analytical modeling presented in Secs. IV and V and agrees well with the model. Other case studies include nonlinear guided waves in tubing to detect creep-fatigue interaction, nonlinear Rayleigh waves to detect susceptibility to stress corrosion cracking, and determination of thermal stress in constrained rail as a warning sign of track buckling.

A. Primary waves are symmetric Lamb waves in plate

The S1–S2 mode pair at internal resonance point 1 (Table III) is the most commonly used nonlinear Lamb wave measurement in a plate.^{27,58,72,78–80} Both the phase and group velocities of the second harmonic match with the primary waves and the mixing power compares favorably to that of bulk wave self-interaction as previously mentioned (15.4 to 24.6 mm^{-2} , respectively). However,

the internal resonance point 1 coincides with a non-leaky point,³⁷ meaning that wave actuation and reception need to involve the in-plane displacement component (u_1), rather than the out-of-plane displacement component (u_3), at the surface of the plate. If angle-beam transducers are selected, they can be coupled by shear couplant or adhesive, but low-viscosity liquid couplant is not recommended. It is difficult to preferentially actuate the S1 mode due to the proximity of other modes, especially the A1 mode, thus a spectrogram obtained from a short-time Fourier transform is more helpful for determining the amplitudes of the primary S1 and secondary S2 modes than is the frequency spectrum obtained from a fast Fourier transform. The cumulative nature of the S2 second harmonic, which has been shown by Bermes *et al.*,²⁷ Matlack *et al.*,⁷² and Liu *et al.*,⁵⁸ is instrumental in distinguishing material nonlinearity from system nonlinearities. The results obtained by Bermes *et al.*²⁷ are shown in Fig. 16. These authors used a 1.6 mm thick plate and a 20-cycle toneburst with a central frequency of 2.15 MHz. The group velocity dispersion curves in Fig. 9(a) show that at $fd = 3.56 \text{ MHz.mm}$ the group

velocities of the S1, A1, A0, S2, S0 modes are 4210, 3050, 3020, 2780, 2470 m/s, respectively. The S1 mode is the first arrival in the A-scan shown in Fig. 16(a), and its amplitude is quite small compared to the later-arriving modes (especially A0 and A1 modes, which arrive almost together). The wave modes can be identified in the Fig. 16(b) spectrogram, which is overlaid upon the group velocity dispersion curves. Moreover, slices taken through the spectrogram at the primary frequency of 2.15 MHz and the secondary frequency of 4.30 MHz enable one to identify the amplitudes of the S1 mode at the primary frequency and the S2 mode at the second harmonic; at approximately $70\ \mu\text{s}$ in Fig. 16(b) since they have the same group velocity. By moving the receiver away from the transmitter the cumulative nature of the second harmonic generation can be shown, as in Fig. 16(c). Bermes *et al.*²⁷ used a laser interferometer, making it easy to move the reception point, but difficult to detect the non-leaky S2 mode. Once confidence is established that the measured nonlinearity is due primarily to the material, then correlation with different material states can be made. Deng and Pei⁸¹ used different primary and secondary Lamb modes to assess fatigue degradation and found that the nonlinearity decreased with fatigue degradation. Pruell *et al.*⁷⁸ demonstrated the effect of plastic deformation (associated with dislocations and slip) in aluminum alloys on the second harmonic, while Pruell *et al.*⁷⁹ demonstrated the effect of low cycle fatigue (associated with persistent slip bands) in an aluminum alloy on the second harmonic, and Metya *et al.*⁸⁰ demonstrated the effect of the tempering temperature (which results in different precipitate size distributions and dislocation densities) on the second harmonic in ferritic steel.

An alternative to the S1–S2 mode pair is the S0–S0 mode pair at low frequencies investigated by Zuo *et al.*⁵⁴ This avoids the problem of multiple modes, but because the frequency is low the power flow is also relatively low, and although they are close, the phase velocities do not exactly match so that rather than being strictly cumulative there are bounded oscillations. In another study, co-directional Lamb wave mixing of the S0 and A1 modes was studied and experiments conducted and the third order harmonics satisfying the internal resonance conditions were observed to be cumulative.⁸²

B. Primary waves are SH waves in plates

The use of SH waves for NDE in plates has lagged behind the use of Lamb waves because SH waves are more difficult to send and receive with piezoelectric transducers. However, SH waves are quite easy to send and receive with magnetostrictive transducers. Here we discuss the use of SH primary waves to generate second order symmetric Lamb waves and third order SH waves.

The fundamental SH wave mode SH0 has the advantages of being nondispersive and having a uniform wavestructure through the thickness. However, there is no power flow to SH waves at the second harmonic frequency as shown in Table II. Power does flow to SH waves at the third harmonic though and results have shown that self-interaction of the SH0 wave mode to generate SH0 waves at the third harmonic are sensitive to plastic deformation⁶⁵ and fatigue.⁶⁶ Since the SH0 mode is nondispersive any excitation frequency can be used, although a frequency below the cutoff frequencies of the other SH modes is preferred to actuate a single mode.

Table III indicates that self-interaction of SH waves generates second harmonic symmetric Lamb waves (internal resonance points 4–8). These self-interactions have high mixing powers as evident from comparing internal resonance points 1 ($15.4\ \text{mm}^{-2}$) and 5 ($22.2\ \text{mm}^{-2}$), which are at the same fd product, making the comparison even more meaningful. Despite the SH2 and S2 modes involved with internal resonance point 5 having different polarities, the mixing power is actually higher than the S1–S2 mode pair. The caveat is that SH2 and S2 group velocities are much different, resulting in separation of the primary and secondary waves and thus a limited mixing zone if a short toneburst excitation is used. Readers may be interested in experiments using internal resonance point 8 presented by Liu *et al.*⁵⁸ Co-directional⁷³ and counter-propagating⁷⁴ wave mixing with SH0 primary waves have shown the sensitivity of mutual interaction induced S0 waves to fatigue degradation.

The next section provides a finite element simulation of nonlinear ultrasonic guided wave propagation, where the primary waves are the SH0 mode and the secondary waves are the S0 mode. The equation formulation in Sec. IV relies on making some key assumptions to provide useful knowledge about nonlinear guided wave propagation. Wave propagation simulations using finite element analysis independent of the assumptions are useful for validating the derived equations. In addition, the results are free from measurement system nonlinearities that exist in the laboratory. We conduct a simulation of nonlinear guided wave propagation in a plate to demonstrate some key aspects of the nonlinearity. The explicit solution technique implemented in the ABAQUS commercial software package is used for the transient dynamics problem. The hyperelastic material model described by Eq. (22) is implemented as a VUMAT in ABAQUS and used to simulate the propagation of SH0 waves. The results show that the SH0 waves generate secondary S0 Lamb waves (internal resonance point 4 in Table III) that increase in amplitude as they propagate as predicted.

1. Model construction

Wave propagation in a nonlinear elastic plate is modeled using three-dimensional C3D8 hexahedral elements that are cubic (0.05 mm per side). Properties representative of aluminum are used: mass density $\rho = 2700\ \text{kg/m}^3$, Lame's constants $\lambda = 51\ \text{GPa}$ and $\mu = 26\ \text{GPa}$, and Landau-Lifshitz parameters $A = -350\ \text{GPa}$, $B = -155\ \text{GPa}$, $C = -95\ \text{GPa}$. The 1-mm thick plate model is 50 mm long. Plane wave propagation is modeled by applying periodic boundary conditions to the lateral surfaces, which enables the discretized domain to be a strip that is just 0.3 mm wide. The top and bottom surfaces are traction-free. The model results are given in terms of the coordinate system shown in Fig. 17, where the wave vector is in the X_1 -direction and the X_3 -direction is through the thickness of the plate. The maximum element length and time step are well within the usual criteria of wavelength/10 and time period/10, respectively. The fundamental SH0 mode is generated by applying a uniform displacement in the X_2 -direction over the end-face at $X_1 = 0$. With respect to time, the applied displacement is a 6-cycle toneburst having a central frequency of 1.68 MHz. This frequency was selected to correspond to internal resonance point 4, where the SH0 and S0 wave modes are synchronized, and additionally, there

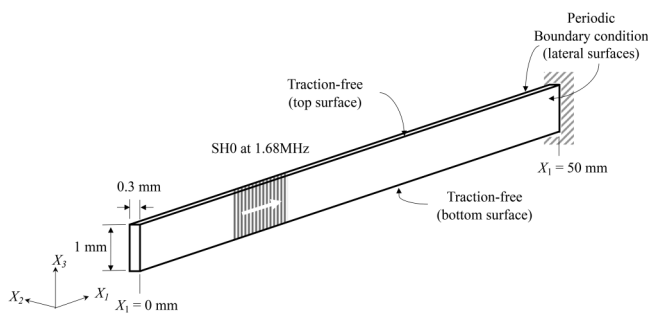


FIG. 17. Finite element model is a vertical slice through a 1 mm thick aluminum plate discretized into $6 \times 20 \times 1000$ elements where the SH0 mode is actuated at $X_1 = 0$.

is nonzero power flow from SH0 waves to second harmonic S0 waves. Thus, the SH0 waves are expected to generate S0 Lamb waves at 3.36 MHz that are cumulative. The wavestructure of a S0 Lamb wave at 3.36 MHz is shown in Fig. 9(c). Note that the u_3 displacement at the surface is relatively large, simplifying detection of the second harmonic. While not shown in a figure in this article, the SH0 wavestructure at all frequencies is simply that $u_2 = \text{constant}$, $u_1 = u_3 = 0$.

2. Second harmonic generation

Snapshots of the wave fields at $t = 5, 10, 15 \mu\text{s}$ are shown in Fig. 18. The u_2 component is associated with the primary SH0 waves, while the u_1 and u_3 components are associated with secondary S0 waves due to self-interaction of the SH0 waves. The u_1 component does not appear to be at 3.36 MHz, which we will discuss later. As confirmation that these displacement components are in fact the SH0 and S0 wave modes, the group velocities are calculated and compared to the dispersion analysis eigen-solutions [Eqs. (16) and (15)] of 3103 m/s and 2376 m/s for the SH0 mode at 1.68 MHz and the S0 mode at 3.36 MHz respectively. The group velocities from the finite element simulation are 3106 m/s for the u_2 component and 2680 m/s for the u_3 component. {For reasons to be described subsequently, the group velocity of the second harmonic is difficult to compute from the finite element results. This value is based on the wave packet peaks received at 15 and 30 mm [Fig. 19(b)].} It is very evident that the displacement components u_1 and u_3 are initially zero but increase with time. A-scans (displacement plotted as a function of time) received at the top surface for $X_1 = 0, 15$, and 30 mm are plotted in Fig. 19 for each displacement component, except that the u_1 component is only shown at 15 mm. Each graph in Fig. 19 provides some new clues about the effect of the material nonlinearity on the nonlinear guided waves. The A-scan of the u_2 displacement component shows that initially (i.e., at 0 mm) the 6 cycles in the wave packet have equal amplitudes. Then at 15 mm and 30 mm the amplitudes of the first and last cycles are reduced, suggesting that the energy in the primary waves is decreasing slightly. The A-scan of the u_3 displacement component clearly increases with propagation distance, as does the number of cycles in the wave packet. At 0 mm the amplitude is

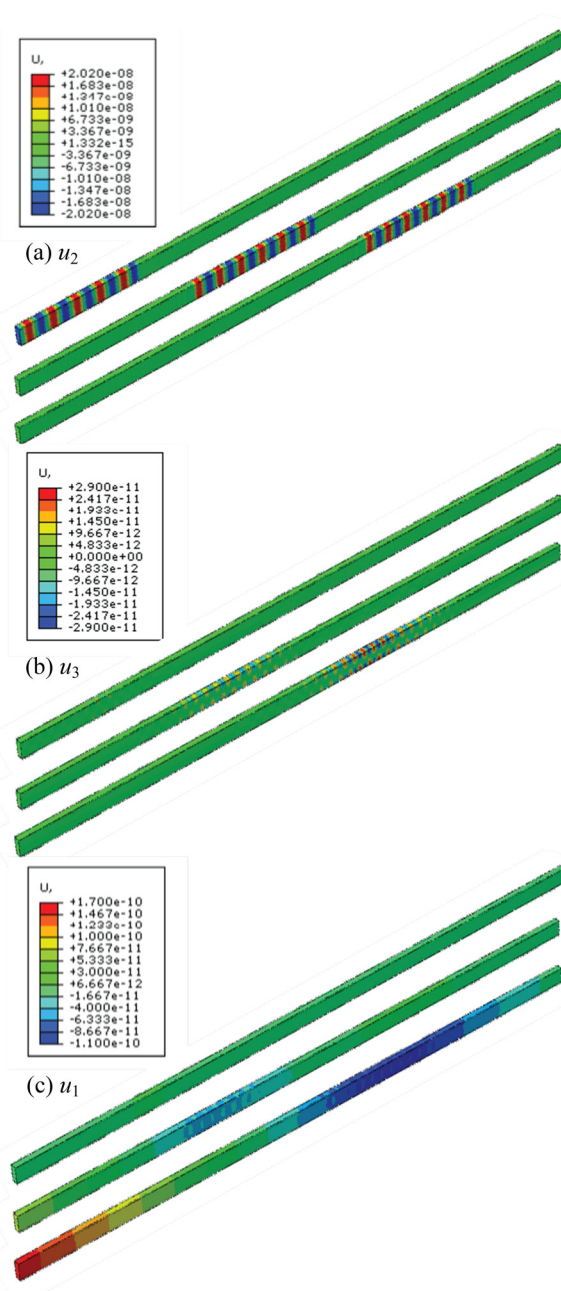


FIG. 18. Snapshots of the wave field at $t = 5, 10, 15 \mu\text{s}$: (a) u_2 component associated with the primary SH0 waves, (b) u_1 and (c) u_3 components associated with the secondary S0 waves. Note the different scales for the different displacement components.

essentially zero, later at 15 mm the peak amplitude is 1.33×10^{-11} m and there are over 18 cycles in the wave packet, then at 30 mm the peak amplitude is 2.66×10^{-11} m and there are over 24 cycles in the wave packet. In addition, the shapes of the waveforms at

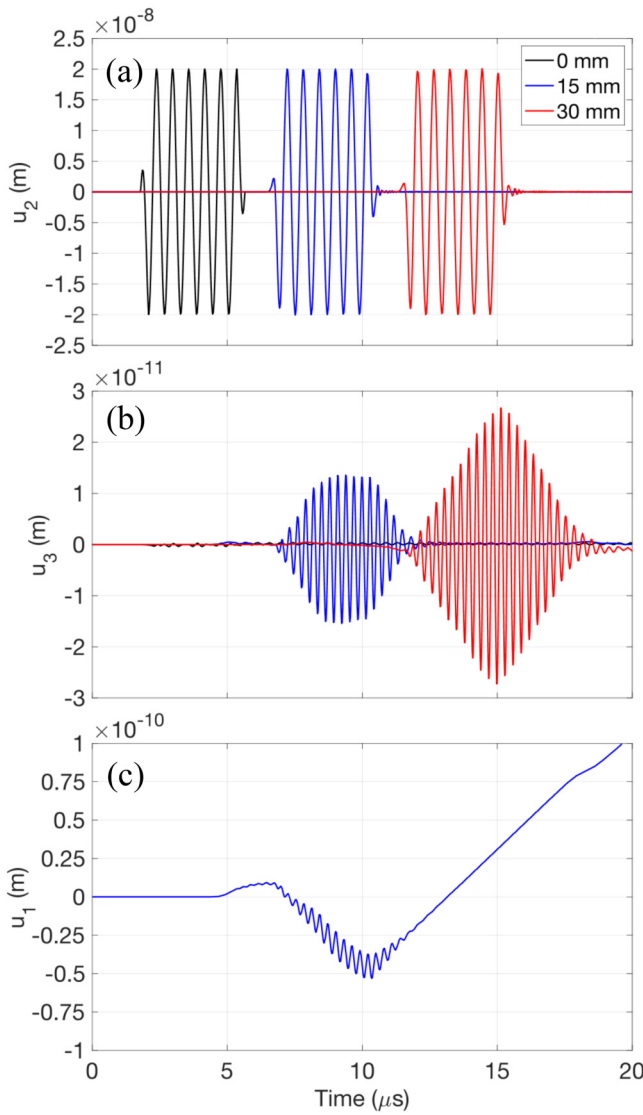


FIG. 19. A-scans received at the top surface for: (a) u_2 component associated with the primary SH0 waves at 0, 15, and 30 mm, (b) u_3 component at 0, 15, and 30 mm and (c) u_1 component at 15 mm associated with the secondary S0 waves. Note the different scales for the different displacement components.

15 mm and 30 mm are considerably different than the flat-top wave packet of the primary waves. At 30 mm, the waveform is almost a diamond shape. The explanation for the increasing number of cycles in the wave packet is that the nonlinear driving forces act like a distributed source for the secondary waves. As the waves interact while propagating, the generated secondary wave packet expands. The A-scan of the u_1 displacement component has an oscillating part superposed on a very low frequency, almost static part. Finally, we point out that the amplitudes of the primary and secondary waves differ by about three orders of magnitude.

The frequency spectra obtained from a fast Fourier transform (FFT) of the wave packets in Fig. 19 are shown in Fig. 20 for each displacement component. The u_2 component is at 1.68 MHz, while the u_3 displacement component is mostly at 3.36 MHz. However, the u_1 component has a low-frequency spectral amplitude (the quasi-static pulse) that overshadows the u_1 component at 3.36 MHz. In cases like this, more sophisticated signal processing such as the empirical mode decomposition^{83,84} could be employed. Thus, the evidence is quite strong that the u_2 component is associated with the SH0 waves at the primary frequency, while the u_1 and

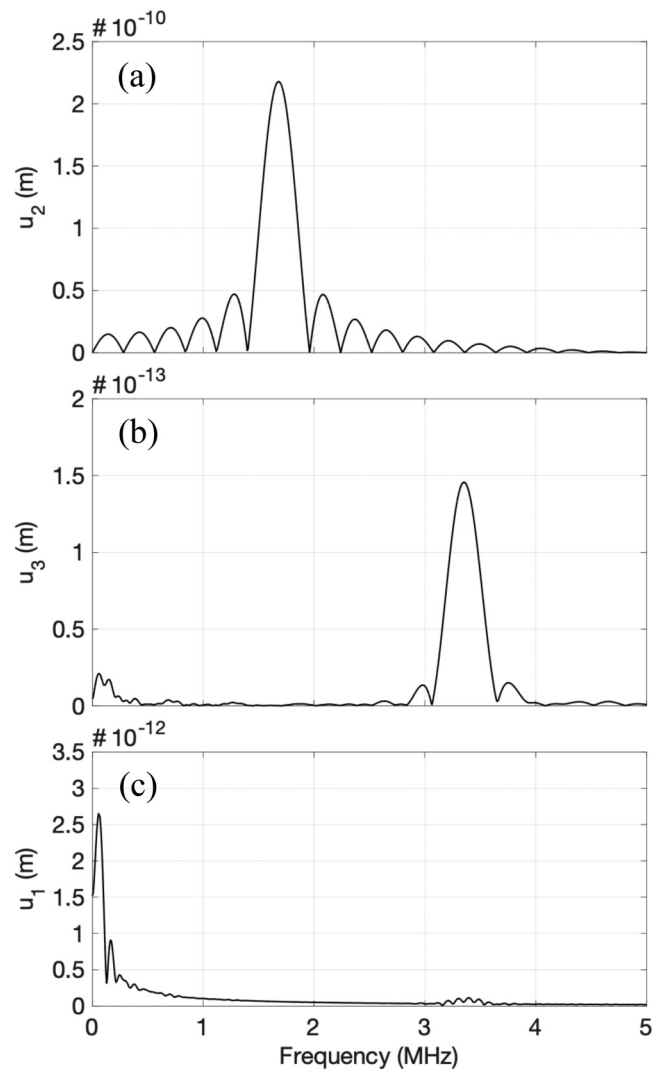


FIG. 20. Frequency spectra obtained from FFT of windowed wave packets received at the top surface for $X_1 = 15$ mm: (a) u_2 component associated with the primary SH0 waves, (b) u_3 and (c) u_1 components associated with the secondary S0 waves. Note the different scales for the different displacement components.

u_3 components are associated with the S0 mode at the second harmonic as well as the quasi-static pulse. The peaks of the wave packets received at 0, 15 mm, and 30 mm are plotted for the u_2 and u_3 displacement components in Fig. 21, which enables us to observe the cumulative behavior of the second harmonic.

We close this section by reiterating that it is customary to quantify the ultrasonic nonlinearity through the relative nonlinearity parameter in Eq. (72), as shown in Figs. 15 and 16(c). However, the evolution in the shape of the secondary wave packet with propagation distance shown in Fig. 19 suggests that the use of β' alone may be insufficient for robust correlation of ultrasonic nonlinearity with material degradation.

3. Energy transfer and power flow

While the perturbation analysis in Sec. IV assumes that the primary wave amplitude remains constant for plane waves in a lossless media, the finite element simulation enables direct assessment of the energy transfer and power flow from primary waves to secondary waves. Both energy transfer and average power flow [P_{mm} in Eq. (39)] from the finite element simulation will now be assessed.

The unique polarizations of the primary SH0 waves, which only have u_2 displacement components, and secondary S0 Lamb waves, which have no u_2 displacement components enable separation of the primary and secondary waves without transforming to the frequency domain. The nonzero Cauchy stress and strain components of the SH0 waves are: $\sigma_{12}, \sigma_{21}, E_{12}, E_{21}$ while for the S0 Lamb waves they are: $\sigma_{11}, \sigma_{33}, \sigma_{13}, \sigma_{31}, E_{11}, E_{33}, E_{13}, E_{31}$. Taking the strain energy density and the power density to be

$$\begin{aligned}\mathcal{E} &= \frac{1}{2} \boldsymbol{\sigma} \mathbf{E}, \\ \mathcal{P} &= \text{Re} \left(-\frac{1}{2} \boldsymbol{\sigma} \mathbf{V}^* \cdot \mathbf{i} \right),\end{aligned}\quad (73)$$

respectively, for wave propagation in the X_1 direction, then for the primary SH0 waves,

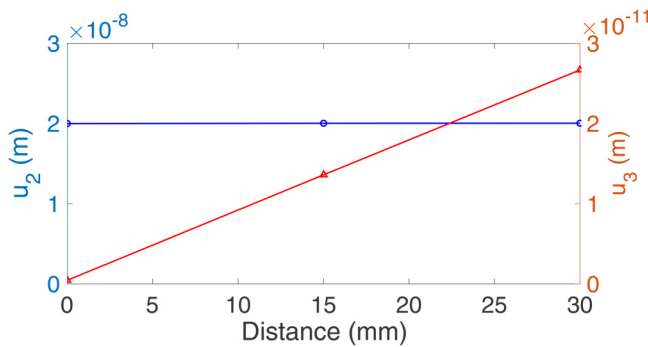


FIG. 21. Wave packet peaks received at 0, 15 mm, and 30 mm: u_2 component in blue associated with the primary SH0 waves and u_3 component in red associated with the secondary S0 waves.

$$\begin{aligned}\mathcal{E} &= \frac{1}{2} [\sigma_{12} E_{12} + \sigma_{21} E_{21}], \\ \mathcal{P} &= \text{Re} \left(-\frac{1}{2} \sigma_{12} V_2^* \right),\end{aligned}\quad (74)$$

while for the secondary S0 waves,

$$\begin{aligned}\mathcal{E} &= \frac{1}{2} [\sigma_{11} E_{11} + \sigma_{33} E_{33} + \sigma_{13} E_{13} + \sigma_{31} E_{31}], \\ \mathcal{P} &= \text{Re} \left(-\frac{1}{2} \sigma_{11} V_1^* - \frac{1}{2} \sigma_{13} V_3^* \right).\end{aligned}\quad (75)$$

In Fig. 22, the strain energy density for SH0 primary waves and S0 secondary waves is plotted as a function of time for receiver locations at 0, 15 mm, and 30 mm. Plots of power density, although not shown, are almost identical in shape. An explanation for the primary wave over-peaks received in the first cycles at 15 and 30 mm does not yet exist. The strain energy density in the secondary waves is six orders of magnitude smaller than in the primary waves and it increases with propagation distance.

The overall energy balance can be assessed by computing the strain energy in the primary waves and in the secondary waves by integrating over the volume of the entire model (120 000 elements). In addition to the nonlinear ultrasonic guided wave model already described, a linear model was also run. The Landau–Lifshitz third

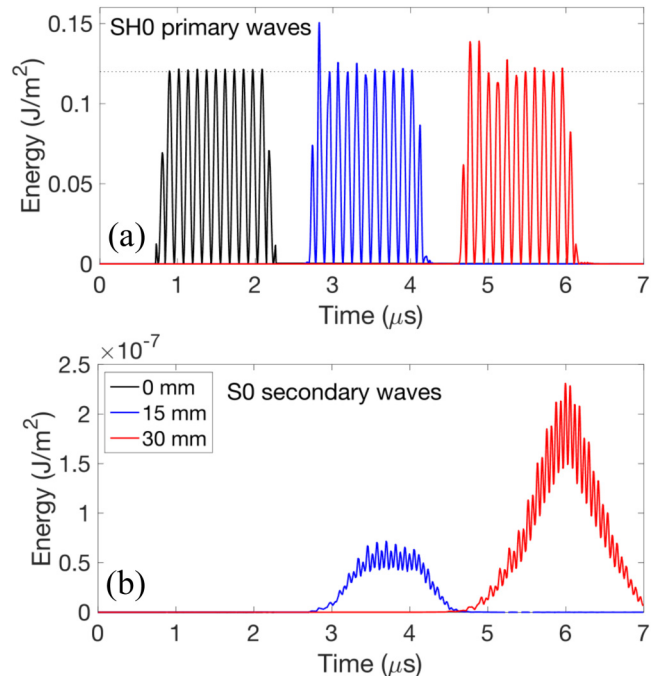


FIG. 22. Strain energy density for (a) SH0 primary waves and (b) S0 secondary waves. The black, blue, and red lines indicate results extracted at $X_1 = 0, 15$, and 30 mm, respectively.

TABLE IV. Total strain energy in the finite element model.

Time (ms)	SH0 primary wavefield (N m)		S0 secondary wavefield (N m)	
	Linear, $\times 10^{-7}$	Nonlinear, $\times 10^{-7}$	Linear, $\times 10^{-22}$	Nonlinear, $\times 10^{-14}$
6.5	3.972 384 757 179 22	3.972 383 913 546 69	1.851 974 629 294 48	3.745 806 501 001 69
9	3.972 376 088 365 80	3.972 372 813 673 15	2.204 868 183 911 38	11.624 338 636 290 5
11.5	3.972 368 429 246 75	3.972 361 755 739 37	2.408 788 376 444 42	22.582 652 414 074 3
14	3.972 360 527 588 94	3.972 349 881 476 17	2.695 506 321 554 89	34.905 929 629 259 2

order parameters were set to zero and the strain–displacement relation was linearized in the linear model. The computed strain energies are given in [Table IV](#) and plotted in [Fig. 23](#). Although integrating over the entire model ensures that all of the energy is accounted for, it results in low energies because the wave energy is

highly localized. The results enable assessment of the premise that the waves are comprised solely of SH0 and S0 waves having the stress and strain components described above. The linear model should have only SH0 waves and the strain energy should be constant for all times. The nonlinear model should show that energy transfers from the SH0 primary waves to the S0 secondary waves. [Table IV](#) and [Fig. 23](#) fulfill these expectations with the exception that the strain energy in the primary waves of the linear model actually decreased. The small decrease could be associated with an increase in stresses and strains other than σ_{12} , σ_{21} , E_{12} , E_{21} due to model imperfections or roundoff errors. The strain energy in the primary waves decreases more in the nonlinear model than in the linear model. Furthermore, there is no increase in the secondary waves in the linear model, while there is in the nonlinear model.

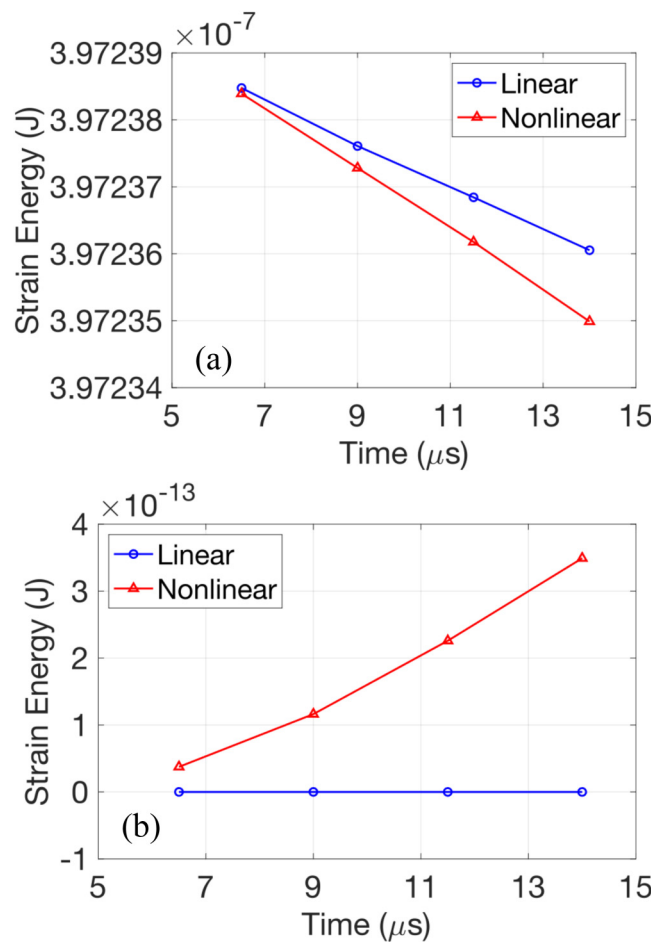


FIG. 23. Total strain energy in finite element model at increasingly larger propagation distances for the (a) SH0 primary waves and (b) S0 secondary waves. The strain energy axes have completely different scales.

C. Axisymmetric waves in tubing

To assess degradation in aluminum tubing, Li and Cho⁸⁵ used the L(0,6)-L(0,10) mode pair, which is akin to internal resonance point 2 in [Table III](#) for Lamb waves in plates. The researchers used wrap-around PVDF comb transducers to send and receive the axisymmetric waves in the pipe and showed that the second harmonic generation was sensitive to thermal damage. Choi *et al.*⁸⁶ used the T(0,1) mode, which is akin to the SH0 mode in a plate, to generate third harmonics to assess creep-fatigue damage to the nickel-based alloy Inconel 617. Magnetostrictive transducers were used to send and receive. For the excitation frequency of 0.83 MHz the results from Choi *et al.*⁸⁶ are summarized in [Fig. 24](#).

Recently, Yeung and Ng⁸⁷ report mixing low frequency T(0,1) waves generated in aluminum tubing with piezoelectric shear transducers and received by a 3D laser Doppler vibrometer. The third order relative nonlinearity parameters increased with increasing fatigue damage.

D. Rayleigh waves in half-space

For NDE applications involving surface waves in thick plates, we will relax our nomenclature and just refer to these as Rayleigh waves. Rayleigh wave inspection is especially useful if the material degradation is expected to initiate at the surface. Jacobs' research group has done extensive work with nonlinear Rayleigh waves. For example, Thiele *et al.*⁸⁸ demonstrate the use of an air coupled transducer to receive nonlinear Rayleigh waves in aluminum samples. Then Marino *et al.*⁸⁹ use this technique to assess ferritic-martensitic steel samples subjected to thermal aging, which is known to dictate the precipitates and dislocation structures upon

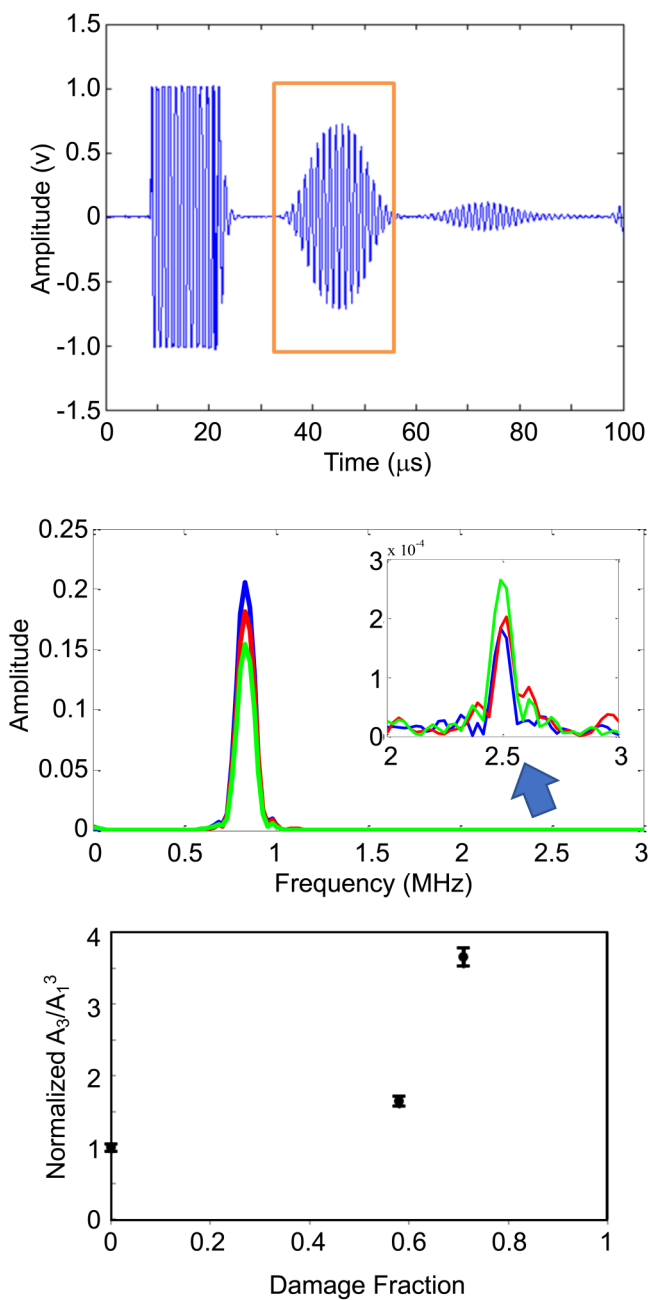


FIG. 24. A-scan, FFT, and increasing relative nonlinearity parameter with creep-fatigue damage. Reproduced with permission from PVP2015-45292 (2015). Copyright 2015 ASME.

which the strength and creep properties are based. The Rayleigh wave measurements showed that the nonlinearity parameter was sensitive to thermal aging even though the linear ultrasonic parameters of velocity and attenuation were quite insensitive. Another

investigation by Doerr *et al.*⁹⁰ assessed the sensitization of austenitic stainless steel, which is due to the precipitation of chromium carbides near grain boundaries. In sensitized material the chromium is depleted at the grain boundaries, making the material susceptible to stress corrosion cracking. These nonlinear Rayleigh wave measurements illustrate that secondary effects, cold work hardening in this case, can also affect the nonlinearity parameter. However, the authors show that annealing removed the work hardening and they were able to clarify the effect that sensitization alone has on the nonlinearity parameter. They were able to confirm the results by making electrochemical measurements.

E. Stress determination in rail

Continuous welded rail is an excellent waveguide that permits ultrasonic waves to travel long distances. The cross-sectional geometry, as shown in Fig. 8, leads to the dense dispersion curves depicted in Fig. 11. Thermal buckling of restrained rail is an insidious failure mode that has proven difficult to predict. A number of nondestructive tests employing acoustoelasticity⁹¹ and diffuse ultrasonic backscatter⁹² have been developed, but Nucera, Lanza di Scalea and co-workers^{31,93} have developed a measurement based on constrained nonlinear wave propagation. The measurement is based on the nonlinearity parameter determined from transducers that send and receive guided waves in the rail. The primary waves are selected based on synchronism and power flux, as well as the wavestructure for excitability purposes. The nonlinearity parameter is a minimum at the neutral temperature, thus increases in the nonlinearity parameter correlate with the temperature offset from the neutral temperature from which the stress can be computed.

IX. CONCLUSION

This Tutorial articulated the principles behind the use of nonlinear ultrasonic guided waves for nondestructive evaluation. It focused on early detection of material degradation but also discussed thermal stress determination and improved reliability with respect to detection of partially closed cracks. The combination of nonlinear ultrasonics and guided waves brings together the capability to detect subtle changes in the microstructure of the material that act as precursors to damage with the ability to make volumetric interrogations from one side of the structure. Numerous structural components are excellent waveguides; e.g., plates, pipes, rods, and rail. Nonlinear ultrasonic inspection of inaccessible structures may be possible with guided waves from two points (through-transmission). The nonlinear ultrasonic techniques described in the Tutorial are most beneficial when linear ultrasonic techniques based on wave speed or wave scattering are inconclusive, which often occurs for early detection of material degradation.

After developing theoretical modeling capabilities, the methodology was summarized for selecting which primary waves to actuate at what frequencies in order to generate cumulative secondary waves. Meeting the internal resonance conditions significantly limits the possibilities. Five case studies were presented to demonstrate application of the principles to make measurements. In one case study, the results from a finite element simulation were presented that showed primary shear-horizontal waves generate cumulative second harmonic waves, which are symmetric Lamb waves.

The results showed the important but minuscule energy transfer from the primary waves to the secondary waves.

As the Tutorial focused on principles of nonlinear ultrasonic guided waves for nondestructive evaluation, it did not address the important topic of correlating the ultrasonic nonlinearity with the material nonlinearity responsible for it. This is a vital aspect of nonlinear ultrasonics, which has been addressed to some extent; see for example, Hikata *et al.*,⁷ Cantrell,⁸ Cash and Cai,⁹ Xiang *et al.*,¹² Li *et al.*,⁹⁵ and Gao and Qu.⁹ In each case, the authors have connected the ultrasonic nonlinearity to some aspect of the material's microstructure. These connections are dependent both on the material and the mode of degradation and are critical to the implementation of nonlinear ultrasonic guided waves for nondestructive evaluation applications. This author sees making connections between the ultrasonic nonlinearity and the material microstructure as fertile ground for future research.

ACKNOWLEDGMENTS

It is imperative for me to recognize the contributions to my understanding of nonlinear guided waves by Yang Liu, Vamshi Chillara, Gloria Choi, Hwanjeong Cho, and Mostafa Hasanian, while they were graduate students at Penn State. Likewise, the ongoing efforts of Anurup Guha and Chaitanya Bakre are greatly appreciated. Many thanks to Hwanjeong Cho for running the finite element simulation in Sec. VIII B. Our research has been supported by the National Science Foundation (NSF) (Nos. 1300562 and 1727292), the Nuclear Energy Universities Program (Nos. 102946 and 120237), and the Vertical Lift Research Center of Excellence at Penn State.

DATA AVAILABILITY

Data sharing is not applicable to this article as no new data were created or analyzed in this study.

REFERENCES

- ¹N. Kawagoishi, Q. Chen, and H. Nisitani, *Fatigue Fract. Eng. Mater. Struct.* **23**, 209 (2000).
- ²I. Y. Solodov, N. Krohn, and G. Busse, *Ultrasonics* **40**, 621 (2002).
- ³P. B. Nagy, *Ultrasonics* **36**, 375 (1998).
- ⁴M. A. Breazeale and D. O. Thompson, *Appl. Phys. Lett.* **3**, 77 (1963).
- ⁵M. A. Breazeale and J. Ford, *J. Appl. Phys.* **36**, 3486 (1965).
- ⁶A. Hikata, B. B. Chick, and C. Elbaum, *Appl. Phys. Lett.* **3**, 195 (1963).
- ⁷A. Hikata, B. B. Chick, and C. Elbaum, *J. Appl. Phys.* **36**, 229 (1965).
- ⁸J. H. Cantrell, *Ultrason. Nondestruct. Eval. Eng. Biol. Mater. Charact.* (CRC Press, 2004), pp. 363–433.
- ⁹X. Gao and J. Qu, *J. Appl. Phys.* **125**, 215104 (2019).
- ¹⁰L. D. Landau and E. M. Lifshitz, *Theory of Elasticity* (Pergamon Press, Tarrytown, NY, 1959).
- ¹¹C. Nucera and F. Lanza di Scalea, *J. Sound Vib.* **333**, 541 (2014).
- ¹²Y. Xiang, M. Deng, C.-J. Liu, and F.-Z. Xuan, *J. Appl. Phys.* **117**, 214903 (2015).
- ¹³R. A. Guyer and P. A. Johnson, *Nonlinear Mesoscopic Elasticity: The Complex Behaviour of Granular Media Including Rocks and Soil* (Wiley-VCH, Weinheim, 2009).
- ¹⁴T. Kundu, *Nonlinear Ultrasonic and Vibro-Acoustical Techniques for Nondestructive Evaluation* (Springer International Publishing, 2019).
- ¹⁵K.-Y. Jhang, C. Lissenden, I. Solodov, Y. Ohara, and V. Gusev, in *Measurement of Nonlinear Ultrasonic Characteristics* (Springer Singapore, 2020).
- ¹⁶R. E. Green, *Ultrason. Investig. Mech. Prop.* (Academic Press, New York, New York, 1973), pp. 73–144.
- ¹⁷A. Norris, *Nonlinear Acoustics* (Academic Press, 1998), pp. 263–278.
- ¹⁸J. L. Rose, *Ultrason. Guid. Waves Solid Media* (Cambridge University Press, 2014), pp. 378–401.
- ¹⁹Y. Zheng, R. G. Maev, and I. Y. Solodov, *Can. J. Phys.* **77**, 927 (1999).
- ²⁰K.-Y. Jhang, *Int. J. Precis. Eng. Manuf.* **10**, 123 (2009).
- ²¹K. H. Matlack, J.-Y. Kim, L. J. Jacobs, and J. Qu, *J. Nondestruct. Eval.* **34**, 273 (2015).
- ²²V. K. Chillara and C. J. Lissenden, *Opt. Eng.* **55**, 011002 (2016).
- ²³W.-B. Li, M.-X. Deng, and Y.-X. Xiang, *Chin. Phys. B* **26**, 114302 (2017).
- ²⁴D. Mingxi, *J. Appl. Phys.* **84**, 3500 (1998).
- ²⁵W. J. N. de Lima and M. F. Hamilton, *J. Sound Vib.* **265**, 819 (2003).
- ²⁶M. Deng, *J. Appl. Phys.* **94**, 4152 (2003).
- ²⁷C. Bermes, J.-Y. Kim, J. Qu, and L. J. Jacobs, *Appl. Phys. Lett.* **90**, 021901 (2007).
- ²⁸M. F. Müller, J.-Y. Kim, J. Qu, and L. J. Jacobs, *J. Acoust. Soc. Am.* **127**, 2141 (2010).
- ²⁹V. K. Chillara and C. J. Lissenden, *J. Appl. Phys.* **111**, 124909 (2012).
- ³⁰Y.-H. Pao, H. Fukuoka, and W. Sachse, *Phys. Acoust.* (Academic Press, Orlando, FL, 1984), pp. 62–144.
- ³¹C. Nucera and F. Lanza di Scalea, *J. Acoust. Soc. Am.* **136**, 2561 (2014).
- ³²B. Dubuc, A. Ebrahimpour, and S. Salamone, *Ultrasonics* **84**, 382 (2018).
- ³³N. Gandhi, J. E. Michaels, and S. J. Lee, *J. Acoust. Soc. Am.* **132**, 1284 (2012).
- ³⁴F. Shi, J. E. Michaels, and S. J. Lee, *J. Acoust. Soc. Am.* **133**, 677 (2013).
- ³⁵A. Pau and F. Lanza di Scalea, *J. Acoust. Soc. Am.* **137**, 1529 (2015).
- ³⁶N. Pei and L. J. Bond, *J. Acoust. Soc. Am.* **140**, 3834 (2016).
- ³⁷J. L. Rose, *Ultrasonic Guided Waves in Solid Media* (Cambridge University Press, Cambridge, 2014).
- ³⁸L. P. Solin and B. A. Auld, *J. Acoust. Soc. Am.* **54**, 50 (1973).
- ³⁹C. Hakoda and C. Lissenden, *Appl. Sci.* **8**, 966 (2018).
- ⁴⁰C. Hakoda and C. J. Lissenden, *J. Sound Vib.* **469**, 115165 (2020).
- ⁴¹Y. Liu, C. J. Lissenden, and J. L. Rose, *J. Appl. Phys.* **115**, 214901 (2014).
- ⁴²L. E. Malvern, *Introduction to the Mechanics of a Continuous Medium*, 1st ed. (Pearson, Englewood Cliffs, NJ, 1977).
- ⁴³Y. Liu, V. K. Chillara, C. J. Lissenden, and J. L. Rose, *J. Appl. Phys.* **114**, 114908 (2013).
- ⁴⁴J. Zhao, V. K. Chillara, B. Ren, H. Cho, J. Qiu, and C. J. Lissenden, *J. Appl. Phys.* **119**, 064902 (2016).
- ⁴⁵A. J. M. Spencer, *Continuum Mechanics* (Courier Corporation, 2012).
- ⁴⁶N. Rauter and R. Lammering, *Int. J. Solids Struct.* **135**, 184 (2018).
- ⁴⁷D. Broda, W. J. Staszewski, A. Martowicz, T. Uhl, and V. V. Silberschmidt, *J. Sound Vib.* **333**, 1097 (2014).
- ⁴⁸I. Solodov, J. Bai, S. Begkulyan, and G. Busse, *Appl. Phys. Lett.* **99**, 211911 (2011).
- ⁴⁹K. Gao, E. Rougier, R. A. Guyer, Z. Lei, and P. A. Johnson, *Ultrasonics* **98**, 51 (2019).
- ⁵⁰B. A. Auld, *Acoustic Fields and Waves in Solids* (John Wiley & Sons Ltd, 1973).
- ⁵¹M. Hasanian and C. J. Lissenden, *J. Appl. Phys.* **124**, 164904 (2018).
- ⁵²N. Matsuda and S. Biwa, *J. Nondestruct. Eval.* **33**, 169 (2014).
- ⁵³V. K. Chillara and C. J. Lissenden, *Ultrasonics* **54**, 1553 (2014).
- ⁵⁴P. Zuo, Y. Zhou, and Z. Fan, *Appl. Phys. Lett.* **109**, 021902 (2016).
- ⁵⁵Y. Liu, E. Khajeh, C. J. Lissenden, and J. L. Rose, *J. Acoust. Soc. Am.* **133**, 2541 (2013).
- ⁵⁶Y. Liu, E. Khajeh, C. J. Lissenden, and J. L. Rose, *J. Appl. Phys.* **115**, 214902 (2014).
- ⁵⁷A. Srivastava and F. Lanza di Scalea, *J. Sound Vib.* **323**, 932 (2009).
- ⁵⁸Y. Liu, V. K. Chillara, and C. J. Lissenden, *J. Sound Vib.* **332**, 4517 (2013).

- ⁵⁹Y. Liu, "Characterization of global and localized material degradation in plates and cylinders via nonlinear interaction of ultrasonic guided waves," (The Pennsylvania State University, 2014).
- ⁶⁰N. Matsuda and S. Biwa, *J. Appl. Phys.* **109**, 094903 (2011).
- ⁶¹M. Deng, P. Wang, and X. Lv, *Appl. Phys. Lett.* **86**, 124104 (2005).
- ⁶²T.-H. Lee, I.-H. Choi, and K.-Y. Jhang, *Mod. Phys. Lett. B* **22**, 1135 (2008).
- ⁶³W. Zhu, Y. Xiang, C.-J. Liu, M. Deng, and F.-Z. Xuan, *Ultrasonics* **90**, 18 (2018).
- ⁶⁴M. Deng, Y. Xiang, and L. Liu, *J. Appl. Phys.* **109**, 113525 (2011).
- ⁶⁵C. J. Lissenden, Y. Liu, G. W. Choi, and X. Yao, *J. Nondestruct. Eval.* **33**, 178 (2014).
- ⁶⁶C. J. Lissenden, Y. Liu, and J. L. Rose, *Insight Non-Destr. Test. Cond. Monit.* **57**, 206 (2015).
- ⁶⁷M. Hasanian and C. J. Lissenden, *J. Appl. Phys.* **122**, 084901 (2017).
- ⁶⁸C. Nucera and F. Lanza di Scalea, *Math. Probl. Eng.* **2012**, 1 (2012).
- ⁶⁹V. Giurgiutiu, *Structural Health Monitoring with Piezoelectric Wafer Active Sensors* (Academic Press, 2007).
- ⁷⁰J. N. Potter, A. J. Croxford, and P. D. Wilcox, *Phys. Rev. Lett.* **113**, 144301 (2014).
- ⁷¹Y. Ohara, T. Mihara, and K. Yamanaka, *Meas. Nonlinear Ultrason. Charact.* (Springer Singapore, n.d.), pp. 165–234.
- ⁷²K. H. Matlack, J.-Y. Kim, L. J. Jacobs, and J. Qu, *J. Appl. Phys.* **109**, 014905 (2011).
- ⁷³S. Shan, M. Hasanian, H. Cho, C. J. Lissenden, and L. Cheng, *Ultrasonics* **96**, 64 (2019).
- ⁷⁴H. Cho, M. Hasanian, S. Shan, and C. J. Lissenden, *NDT E Int.* **102**, 35 (2019).
- ⁷⁵C.J. Lissenden, Y. Liu, V.K. Chillara, G. Choi, and X. Yao, in *Proc. ASME 2014 Int. Mech. Eng. Congr. Expo.* (Montreal, Canada, 2014), pp. IMECE2014-39399.
- ⁷⁶J.-Y. Kim, L. J. Jacobs, J. Qu, and J. W. Littles, *J. Acoust. Soc. Am.* **120**, 1266 (2006).
- ⁷⁷S. Shan, L. Cheng, and P. Li, *Smart Mater. Struct.* **26**, 025019 (2017).
- ⁷⁸C. Pruell, J.-Y. Kim, J. Qu, and L. J. Jacobs, *Appl. Phys. Lett.* **91**, 231911 (2007).
- ⁷⁹C. Pruell, J.-Y. Kim, J. Qu, and L. J. Jacobs, *Smart Mater. Struct.* **18**, 035003 (2009).
- ⁸⁰A. K. Metya, M. Ghosh, N. Parida, and K. Balasubramaniam, *Mater. Charact.* **107**, 14 (2015).
- ⁸¹M. Deng and J. Pei, *Appl. Phys. Lett.* **90**, 121902 (2007).
- ⁸²W. Li, M. Deng, N. Hu, and Y. Xiang, *J. Appl. Phys.* **124**, 044901 (2018).
- ⁸³N. E. Huang, Z. Shen, S. R. Long, M. C. Wu, H. H. Shih, Q. Zheng, N.-C. Yen, C. C. Tung, and H. H. Liu, *Proc. R. Soc. Lond. Ser. Math. Phys. Eng. Sci.* **454**, 903 (1998).
- ⁸⁴Y. Lei, J. Lin, Z. He, and M. J. Zuo, *Mech. Syst. Signal Process.* **35**, 108 (2013).
- ⁸⁵W. Li and Y. Cho, *Exp. Mech.* **54**, 1309 (2014).
- ⁸⁶G. Choi, Y. Liu, and C.J. Lissenden, in *Proc. ASME 2015 Press. Vessels Pip. Conf.* (American Society of Mechanical Engineers Digital Collection, Boston, Massachusetts, 2015), pp. PVP2015-45292.
- ⁸⁷C. Yeung and C. T. Ng, *J. Sound Vib.* **485**, 115541 (2020).
- ⁸⁸S. Thiele, J.-Y. Kim, J. Qu, and L. J. Jacobs, *Ultrasonics* **54**, 1470 (2014).
- ⁸⁹D. Marino, J.-Y. Kim, A. Ruiz, Y.-S. Joo, J. Qu, and L. J. Jacobs, *NDT E Int.* **79**, 46 (2016).
- ⁹⁰C. Doerr, J.-Y. Kim, P. Singh, J. J. Wall, and L. J. Jacobs, *NDT E Int.* **88**, 17 (2017).
- ⁹¹M. Hirao, H. Ogi, and H. Fukuoka, *Res. Nondestruct. Eval.* **5**, 211 (1994).
- ⁹²C. M. Kube, H. Du, G. Ghoshal, and J. A. Turner, *J. Acoust. Soc. Am.* **132**, EL43 (2012).
- ⁹³C. Nucera, R. Phillips, F. L. di Scalea, M. Fateh, and G. Carr, *Transp. Res. Rec. J. Transp. Res. Board* **2374**, 154 (2013).
- ⁹⁴W. D. Cash and W. Cai, *J. Appl. Phys.* **109**, 014915 (2011).
- ⁹⁵Y. Li, S. Hu, and C. H. Henager, *J. Appl. Phys.* **125**, 145108 (2019).